6-28-2013

Investigation of thermal properties and latent heat reduction mechanisms in nanofluid phase change materials

Aitor Zabalegui
Santa Clara University

SANTA CLARA UNIVERSITY

Department of Mechanical Engineering

Date: June 28, 2013

I HEREBY RECOMMEND THAT THE THESIS PREPARED UNDER MY SUPERVISOR BY

Aitor Zabalegui

ENTITLED

INVESTIGATION OF THERMAL PROPERTIES AND LATENT HEAT REDUCTION MECHANISMS IN NANOFLUID PHASE CHANGE MATERIALS

BE ACCEPTED IN PARTIAL FULFILLMENT OF THE REQUIREMENTS FOR THE DEGREE OF

MASTER OF SCIENCE IN MECHANICAL ENGINEERING

_____

Thesis Advisor

_____

Chairman of Department

INVESTIGATION OF THERMAL PROPERTIES AND LATENT HEAT REDUCTION MECHANISMS IN NANOFLUID PHASE CHANGE MATERIALS

By
Aitor Zabalegui

MASTER THESIS

Submitted in Partial Fulfillment of the Requirements
For the Degree of Master of Science
In Mechanical Engineering
In the School of Engineering at
Santa Clara University, June 2013

Santa Clara, California

ACKNOWLEDGEMENTS

This research was supported by Lawrence Berkeley National Laboratory and the School of Engineering, Center for Science, Technology, and Society, and the Sustainability Research Initiative at Santa Clara University.

I would like to thank the guidance, support, and patience of Dr. Hohyun Lee, whose unwavering determination as an advisor elevated my research to a higher standard. Dr. Lee offered me novel and compelling research when forced to change projects, and assured my continued financial support. He was also responsible for introducing me to Dr. Daniel Strickland, to whom I would also like to express my respect and gratitude. Dr. Strickland initially took me on as his research assistant, allowing me to grow and develop as an engineer within the master's program at Santa Clara University. He will always be remembered and missed.

I wish to thank the School of Engineering for sponsoring my graduate education, and providing me the opportunity to work as a Teaching Assistant. Additionally, I would like to thank faculty members Dr. Prashanth Asuri and Dr. Abdie Tabrizi for their assistance and support over the course of my graduate research. I also wish to extend my thanks to Dr. Ilir Beta and Brian Ricks at NETZSCH Instruments in Boston for their training and technical assistance during my visit.

I would like to express my thanks and admiration for my fellow graduate researchers and classmates: Shawn Tokairin, Miguel Gomez, Leejay Hsu, Sandeep Lele, Michael Sizemore, Marcial Portilla, Matthew Neber, Kalpith Ramamoorthi, and John O'Malley. Lastly, I wish to thank my family and friends. Specifically, Nicole Papetti for

her emotional support; Orion Ashmore for inspiring me to challenge myself and helping to shape my character; The Fiends, whom I am proud to have as friends; and finally, my parents for their unconditional selflessness and generosity. I owe any opportunities for success to you.

Table of Contents

List of Tables

List of Figures

Nomenclature

A	Avogadro's number [mol^{-1}]
A_s	Surface area [m^2]
C	Proportionality constant
c_p	Specific heat [J/kg·K]
D	Diffusion length [m]
d	Nanoparticle diameter [m]
d_f	Fractal dimension [m]
DSC	DSC unit [W/g]
E	Enthalpy [J/m^3]
h	Latent heat of fusion [J/g]
k	Thermal conductivity [W/m·K]
k_c	Collision rate [$s^{-1}m^{-3}$]
k_B	Boltzmann constant [m^2kg/s^2K]
L	MWNT length [m]
m	Mass [kg]
N	Number density [m^{-3}]
n	Sphericity variable
Q	Net heat transfer [W]
q	Collision frequency [s^{-1}]
q''	Heat flux [W/m^2]
R	Universal gas constant [J/molK]
r	Pearson correlation coefficient
R_a	Radius of gyration [m]
R_{bd}	Kapitza resistance [m^2K/W]
T	Temperature [K]
t	Time [sec]
U	Internal energy [W]
V	Volume [m^3]
w	Interface phase width [m]
wp	Weight percent
x	Position [m]
x^2	Mean square displacement [m^2]
Greek symbols	
α	Thermal diffusivity [mm^2/s]
λ	Average Brownian diffusion length [m]

μ	Dynamic viscosity [N·s/m^2]
ρ	Density [g/cm^3]
σ	Latent heat reduction rate [m^{-1}]
τ	Collision time scale [sec]
ϕ	Volume fraction
Ψ	Sphericity

Subscripts

∞	Ambient
1/2	Half time
a	aggregate cluster
b	Base molecule
b-p	Collision between base molecule and particle
bf	Base fluid
BrS	Brownian sweep volume
c	Collision
DPL	Densely packed layer
eff	Effective
f	Fluid
HC	Hamilton-Crosser theory
HS, low	Hashin-Shtrikman lower bound
HS, up	Hashin-Shtrikman upper bound
i	Interface
i+p	Sum of interface layer and particle
init	initial
int	Particles in the cluster
j	Finite element node position
l	Liquid
Max	Maxwell theory
max	Maximum
melt	Melting
N	Final node
Nan	Nan et al.'s theory
nf	Nanofluid
p	Nanoparticle
PCM	Phase change material
r	Finite element step size
req	Required to fit measured latent heat
sl	Solid-liquid phase change

sp	Strained phase
std	Standard
tern	Ternary nanofluid
wf	Working fluid

Superscripts

i	Iterative time step

ABSTRACT

The thermal properties of paraffin-based nanofluids have been examined to investigate the use of enhanced phase change materials (PCMs) for thermal energy storage (TES). PCMs are promising for TES applications, but low thermal conductivity limits their rate of heat exchange with a working fluid. The nanofluid approach has been established as a method of thermal conductivity enhancement, but effects of particle addition on other thermal properties affecting TES are relatively ignored. Significant reduction in latent heat of fusion below traditional effective medium theory has been observed in nanofluids. An experimental study of paraffin nanofluids, containing various diameter multi-walled carbon nanotubes, has been conducted to investigate these findings. Results demonstrate that the magnitude of nanofluid latent heat reduction increases for smaller diameter particles in suspension. A method to approximate nanofluid latent heat of fusion is presented, considering the diameter-dependent reduction observed. Three possible mechanisms – interfacial liquid layering, Brownian movement, and particle clustering – are examined to explain further reduction in latent heat, through weakening of molecular bond structure. Although interfacial layering effects and Brownian motion contribute some reduction, experimental evidence suggests that particle clustering is the only mechanism capable of explaining the degree of latent heat reduction observed. Additional research is needed to explore these proposed mechanisms. Nanofluid latent heat and effective thermal conductivity were analyzed collectively to investigate the effects of particle size on PCM energy storage performance. It is shown that while particle diameter significantly impacts nanofluid latent heat, thermal conductivity exhibits a negligible size dependency. Governing equations for a finite element model of nanofluid phase change is presented, as a method of quantifying PCM energy storage performance. Measured and approximated thermal properties from this study can be applied as model parameters to size an appropriate storage container for TES applications. The future model will serve as a predictive tool for determining optimum particle diameter and volume fraction to maximize energy stored and extracted over a given period of time.

Chapter 1

Introduction

Solar thermal energy is an abundant, clean, and practical renewable energy source. For instance, solar thermal collectors can utilize the full spectrum of solar radiation, absorbing most incident light with minimal thermal radiation emission. Since any wasted heat can be recycled in cogeneration processes, solar thermal energy exhibits high theoretical efficiency. In high temperature applications, solar thermal can convert solar energy to electricity more efficiently than photovoltaics. Despite the benefits of solar thermal energy, its availability is not always synchronized with peak hours of energy demand. Peak energy demand is usually highest in winter or after sunset, coinciding with the lowest levels of solar radiation. With thermal energy storage (TES), excess thermal energy during off-peak hours may be utilized during subsequent peak demand hours to offset the mismatch of availability and demand [1]. In utility applications such as concentrated solar power (CSP) plants, for example, high-temperature salt eutectics are used to store thermal energy in the form of sensible heat, with a storage capacity of up to 7 hours [2]. When a CSP system has cooled overnight, its power generation is delayed upon restarting by having to heat the entire system to working temperature. Therefore, a thermal storage system can be utilized to keep the system at operable temperature, continuously meet base load demands, and improve power generation efficiency.

On the residential scale, TES can be utilized for domestic water heating, space heating, or waste heat recovery [3-5]. Phase change materials (PCMs) are promising for TES, due to several advantageous physical and thermal properties. For example, organic

PCMs such as paraffin wax are available in a large range of melting temperatures, are chemically stable and recyclable, and show good compatibility with other materials [6]. The primary advantage of PCMs is their high specific energy storage capacity. Large quantities of thermal energy may be stored or extracted in latent heat of fusion and crystallization, respectively. Paraffin wax exhibits a latent heat of fusion of nearly 200 kJ/kg [7]. Although these properties are ideal for TES, PCMs typically exhibit low thermal conductivity, which limits their rate of heat exchange with a working fluid or other heat transfer medium. Due to this low charge/discharge rate, PCMs in TES systems may not meet energy demand over given periods of time, and thus, will require larger heat exchangers. Many methods of improving PCM thermal conductivity have been developed, including nano-encapsulation [8, 9], modification of PCM container structure [10-12], and suspension of highly thermally conductive nanoparticles [13-15].

Encapsulation involves surrounding PCM with a protective shell to prevent aggregation and precipitation during phase change. The shell is composed of an impermeable polymer or metallic material and provides a high surface area to volume ratio, which enhances heat transfer into the PCM. Nano-encapsulation is typically utilized to enhance the heat capacity of heat transfer fluids for cooling applications, but also introduces higher pumping costs due to increased viscosity [16]. On the other hand, PCM storage container structure can be modified with the addition of fins, wire meshes, or carbon fiber brushes to increase heat transfer area [11, 17]. The majority of research for this method focuses on optimal configurations and orientation of extended surfaces, through experimental and numerical study [10, 18]. Although considerable heat transfer

enhancement has been demonstrated, storage container modification requires complex manufacturing and reduces available PCM volume.

Dispersions of highly conductive nanoparticles, such as Al_2O_3, copper, graphite, or carbon nanotubes, into a base fluid are known as nanofluids. Significant thermal conductivity enhancement has been reported in nanofluids, even at low particle volume fractions [19]. However, it has also been shown that nanoparticle addition causes a greater increase in viscosity than the enhancement of thermal conductivity [20]. Although Prasher et al. [21] report that nanofluid viscosity enhancement must be at least a factor of four times greater than conductivity enhancement to have a negative impact on thermal performance, high viscosity is generally not beneficial for heat transfer fluids. Therefore, nanofluid PCMs may be more applicable for stationary TES applications, since high viscosity will not have such a detrimental effect.

Although it is well-established that nanofluids exhibit enhanced thermal conductivity, the degree of enhancement is controversial [22, 23]. Nanofluid thermal conductivity effective medium theory (EMT) was originally described by Maxwell [24] for well-dispersed, spherical particles. Numerous studies have investigated potential mechanisms to describe anomalous thermal conductivity enhancement beyond traditional Maxwell EMT. Four primary mechanisms were considered as highly probable influences:

- Brownian motion induces micro or nano-convection effects in the base fluid, which increase heat transfer.
- Liquid layering effects create more ordered, crystalline layers at particle interfaces, which increase the effective volume of high conductivity phase.

- The nature of heat transport on the nanoscale, where ballistic phonon transport from particle to particle increases thermal conductivity.
- Nanoparticle clustering, where particle aggregation forms high aspect ratio clusters with high conductivity pathways for enhanced heat transfer.

A common assumption in theoretical analysis of particle suspension conductivity is that dispersed particles are essentially motionless in a heterogeneous solid/fluid mixture. It was previously believed that at very small particle sizes, as in nanofluids, Brownian motion assumes a significant role in energy transport [25-27]. Brownian motion describes the random movement of particles in a fluid, which result in particle collisions that facilitate energy transfer through direct, solid-to-solid interaction [28]. Brownian particle diffusion was suggested to generate a velocity field in the surrounding base fluid that decays outward as the inverse of the distance from the particle center [23]. The large volumes of fluid dragged by Brownian particles carry a significant amount of heat. Thus, Brownian motion was proposed to induce micro or nanoconvection effects, which could explain nanofluid thermal conductivity enhancement. However, the time scale for Brownian diffusion is orders of magnitude longer than the time scale for heat diffusion, even when considering molecule-sized particle diameters. Therefore, it has been concluded the time scale of Brownian motion is too slow to play a significant role in conductivity enhancement [29]. Furthermore, microconvection models developed by Jang and Choi [25] and Prasher et al. [27] have shown direct conflict with experimental evidence [30, 31] and molecular dynamics simulations [32], which demonstrate that Brownian motion cannot explain reported conductivity enhancement.

Liquid layering effects describe the ordering of base fluid molecules at the nanoparticle interface, drawn to particle surfaces by van der Waals forces. It was initially suggested that the more crystalline structure of densely packed molecules at the particle interface exhibit improved thermal properties [29, 33], which was expected to result in thermal conductivity enhancement. Ordered molecules at the interface increase the effective volume of high conductivity phase within the nanofluid, and thus, could explain enhancement with traditional EMT. However, subsequent experimental studies [34] and molecular dynamics simulation [35] show that the ordered liquid layer width is no larger than a few molecular spacings, or on the order of 1-2 nm from the particle surface. The small volumes of ordered base fluid within interfacial layers will have a negligible influence on nanofluid thermal transport, and cannot explain the degree of thermal conductivity enhancement observed [29].

The nature of heat transport on the nanoscale refers to the invalidity of applying macroscopic theories to describe diffusive heat transport in nanofluids. In crystalline solids, heat is generally transferred diffusely by phonon propagation and scattering. However, with sufficiently small particles, the phonon mean free path becomes longer than the diameter of the particle, and phonons travel ballistically through the solid [29, 36]. In order for ballistic transport to substantially influence nanofluid thermal conductivity, ballistic phonons must transfer from particle to particle without significant scattering in the liquid. Since the mean free path in the liquid is much shorter than in the solid, particle to particle ballistic transport is only possible with very small separation between particles, on the order of 1-2 nm. The concept of high particle packing density leading to thermal

conductivity enhancement is addressed by the final proposed enhancement mechanism, nanoparticle clustering.

Average inter-particle distance decreases for smaller diameter particles in suspension. Particles situated closer together will experience a stronger attraction due to van der Waals forces, and thus, are more likely to aggregate [37]. Aggregated particles form high aspect ratio clusters which facilitate high conductivity percolation pathways for heat transfer; however, there is a limit to the beneficial effect of cluster formation on thermal conductivity. With significant particle aggregation, especially at low volume fractions, large clusters will settle out of the base fluid and create particle free regions of high thermal resistance [29]. There is a maximum possible thermal conductivity enhancement effect between no aggregation and complete aggregation, where loose cluster formation is favorable due to the larger effective volume of high conductivity phase. Clusters with low packing fractions and large effective particle volumes have been demonstrated as a capable explanation for experimentally observed thermal conductivity enhancement [37].

Given that aggregation and particle geometry has a significant effect on thermal conductivity enhancement, the simplifying assumptions of spherical, evenly-dispersed particles in traditional Maxwell EMT cannot accurately describe effective thermal conductivity for all nanofluids. Thus, anomalous nanofluid thermal conductivity enhancement may simply be due to inapplicable comparison to Maxwell's EMT. A comprehensive study of nanofluid thermal conductivity, including measurements from 31 international organizations, was conducted as an exercise to address uncertainties in different measurement techniques and nanofluid parameters [22]. It was thought that

systematic differences such as particle shape led to discrepancies in reported thermal conductivity values. Although nanofluids with near-spherical particles exhibited thermal conductivities that were in good agreement with traditional Maxwell EMT, elongated particles tested displayed additional thermal conductivity enhancement beyond Maxwell's theory. The additional enhancement for elongated particles was reported as repeatable within a relatively narrow ±10 % band, and was well-described by modified EMT for high aspect ratio particles [38]. Therefore, it was concluded that anomalously reported thermal conductivity enhancement was not only attributed to discrepancies in nanofluid fabrication and measurement methods, but was primarily due to comparison with inappropriate EMT.

Numerous modified EMTs have been developed to account for non-spherical particles, high particle aspect ratio, and Kapitza resistance, which are not included in traditional Maxwell theory. The Hashin-Shtrikman bounds [39, 40], Hamilton-Crosser theory [41], and Nan et al.'s model [38, 42], have shown good agreement with reported nanofluid thermal conductivity and elucidate anomalous findings. An explanation of these theories, along with Maxwell's equation for effective thermal conductivity, is provided in Chapter 2.

Although considerable research efforts have focused on nanofluid thermal conductivity, other thermal properties affecting TES, such as specific heat capacity or latent heat of fusion, do not receive as much attention. Specific heat capacity is commonly believed to not exhibit any nanoscale effects [43], but recent experimental findings by Shin and Banerjee [44, 45] and Wang et al. [46] show significant heat capacity enhancement in nanostructures and nanofluids. Shin and Banerjee proposed that the observed nanofluid heat capacity enhancement was due to improved thermal properties of semi-solid layers at

particle interfaces, formed by liquid layering effects.On the other hand, nanofluid latent heat of fusion is expected to linearly decrease as particles not contributing to phase change are added to the base fluid [47, 48]. However, several experimental studies on nanofluids have reported additional reduction beyond latent heat EMT. Wu et al. [47] reported a nearly 10 % drop from expected latent heat of Cu/paraffin nanofluids with 25 nm diameter particles at 1 % volume fraction. Zeng et al. [49] observed a similar reduction at 1 % volume fraction with copper nanowires in tetradecanol. Ho and Gao [50] reported a less significant reduction of approximately 3 % for alumina-in-paraffin emulsions, with 177.8 nm diameter particles at 2 % volume fraction. Despite the similarity of these observations and their inconsistency with theory, latent heat characterization was not the intended focus of these studies, and no possible reduction mechanisms were suggested. However, Wu et al. [47] proposed that a new model for latent heat EMT of solid-liquid mixtures is needed. From the reported findings, it is apparent that nanofluids of smaller particle diameter exhibit greater reduction in latent heat of fusion. Studies to investigate this relationship have yet to be conducted.

As mentioned previously, nanofluid latent heat reduction is defined by the mass – or volume – of particles within the nanofluid that do not contribute to phase change. Therefore, latent heat reduction beyond EMT suggests that other than the volume of suspended particles, there is additional nanofluid volume not contributing to phase change. It is postulated that molecular strain induced by various interface phenomena facilitates latent heat reduction by weakening base fluid molecular structure. Volumes of strained bond structure will require less energy to break down during melting; and thus, should account for additional volume not contributing to phase change. The interface phenomena

considered: interfacial liquid layering, Brownian motion, and particle clustering, are all diameter-dependent mechanisms that have varying contributions to latent heat reduction. Liquid layering, for example, generates molecular strain in the base fluid surrounding ordered layers formed at the particle interface. The total liquid layer volume in a nanofluid is dependent on interface density, which increases for smaller particles in suspension. Brownian motion should also facilitate latent heat reduction by generating pathways of weakened bond structure; an effect that becomes more vigorous with smaller particles. Lastly, smaller particles in suspension are more likely to aggregate, weakening bond structure as particles migrate into high aspect ratio clusters. Therefore, it is hypothesized that latent heat reduction is diameter-dependent, with smaller diameter particles producing greater degrees of reduction. Characterization of nanofluid latent heat with respect to particle diameter is needed to explore observable trends and investigate the reduction mechanisms described.

Since most TES applications require energy to be stored or released in a given amount of time, storage performance can be evaluated as how much energy is transferred over a given duration. Changes in both thermal conductivity and latent heat of fusion will affect storage performance simultaneously. While enhanced thermal conductivity improves heat transfer rate, reduced latent heat decreases specific energy storage capacity. Although reduced latent heat can also increase energy charge/discharge rate, due to shortened melt time, greater nanofluid PCM volume will be required to account for reduced storage capacity.

Thermal diffusivity, defined as the area to which heat is transferred per unit time, also plays a significant role in storage performance. According to traditional EMT,

nanofluid thermal diffusivity should demonstrate enhancement similar to or greater than thermal conductivity – since specific heat is expected to decrease with particle addition, while density shows a negligible increase. Detailed EMT derivations for these thermal properties are given in Chapter 2. Increased thermal diffusivity will directly impact energy charge/discharge rate, transferring energy more quickly to and from greater areas of nanofluid PCM. Consequently, recently reported nanofluid specific heat capacity enhancement suggests that particle addition should have an adverse effect on thermal diffusivity. Therefore, it is important to consider effects of particle addition on all nanofluid thermal properties affecting TES performance.

In this thesis, a comprehensive characterization study of nanofluid thermal properties has been conducted, utilizing differential scanning calorimetry (DSC) and laser flash analysis (LFA). Nanofluids, consisting of various diameter multi-walled carbon nanotubes (MWNTs) dispersed in paraffin wax, were examined to assess effects of particle addition on nanofluid thermal conductivity, latent heat of fusion, specific heat capacity, and thermal diffusivity. Resulting thermal properties are compared to traditional and modified EMTs, and support three separate analyses:

- The effect of particle diameter on nanofluid latent heat of fusion is investigated. The proposed reduction mechanisms described: interfacial liquid layering, Brownian motion, and particle clustering are explored with respect to measured results. It is concluded that nanofluid latent heat of fusion is significantly dependent on particle diameter, with reduction magnitudes increasing for smaller diameter particles in suspension. In addition, Brownian motion and liquid layering are demonstrated as incapable of solely accounting for the degree of latent heat

reduction observed. Particle clustering is suggested as the principle mechanism for latent heat reduction, but further investigation is needed.

- A method of approximating nanofluid latent heat is presented, considering the diameter-dependent reduction observed.
- Effects of nanoparticle size and volume fraction on nanofluid PCM storage performance are studied. Utilizing Nan's EMT, it is shown that particle diameter has a negligible effect on thermal conductivity, in contrast to the significant diameter-dependency of latent heat of fusion. A numerical model of nanofluid phase change is suggested as a predictive tool to determine optimum particle diameter, volume fraction, and PCM container size to maximize TES storage performance. Governing discretized equations and boundary conditions are presented. Measured and approximated nanofluid thermal properties may be applied to future implementation of the proposed modeling study.

Chapter 2

Nanofluids: Background and Effective Medium Theory

Introduced by Choi and Eastman [51] nearly twenty years ago, the nanofluid approach for enhanced thermal conductivity has drawn considerable interest in the research community. Despite continued efforts to improve their thermal transport properties, nanofluids have yet to be commonly employed in commercial heat transfer applications. There are several fundamental barriers that prevent nanofluids from bridging the gap between research and commercial application [52, 53]:

- Lack of a predictive understanding of thermal and physical properties. Contradictory findings in literature hinder the development of a comprehensive theory to explain energy transfer processes in nanofluids.
- The need for an experimental database of nanofluid parameters, preparation and measurement techniques, and thermo-physical properties.
- Application-based requirements such as long-term stability, high thermal conductivity with minimal viscosity increase, the use of environmentally benign materials, and cost-effectiveness.

Collective studies such as the International Nanofluid Property Benchmark Exercise (INPBE)[22] are essential to forming a standardized database of nanofluid properties and preparation methods, which will improve the practicality of these materials. The INPBE highlighted many of the experimental inconsistencies in nanofluids research, and showed that the majority of reported anomalously enhanced thermal conductivity was due to inappropriate comparison to traditional Maxwell EMT. This chapter provides an overview

of Maxwell's theory for effective nanofluid thermal conductivity, and presents several modified effective medium theories which can explain the anomalous behavior reported in nanofluids research. In addition, the derivation of equations for effective nanofluid thermo-physical properties, including density, specific heat, thermal diffusivity, and latent heat of fusion, are also presented.

2.1 Maxwell's Effective Medium Theory

Developed over a century ago to describe dielectric properties of composite materials [24], Maxwell's theory for evenly-dispersed, spherical particles at low particle loadings is commonly expressed as:

$$\frac{k_{eff,Max}}{k_{bf}} = \frac{k_p + 2k_{bf} + 2\phi_p(k_p - k_{bf})}{k_p + 2k_{bf} - \phi_p(k_p - k_{bf})} \tag{2.1}$$

where ϕ is volume fraction and k is thermal conductivity, with *eff*, *p*, and *bf* denoting properties of the effective mixture, nanoparticle, and base fluid, respectively. Equation 1 can be expressed in a more practical form, given by:

$$\frac{k_{eff,Max}}{k_{bf}} = \frac{k_p(1+2\phi_p) + 2k_{bf}(1-\phi_p)}{k_p(1-\phi_p) + k_{bf}(2+\phi_p)} = 1 + \frac{3\phi_p\left(\frac{k_p}{k_{bf}} - 1\right)}{\left(\frac{k_p}{k_{bf}} + 2\right) - \phi_p\left(\frac{k_p}{k_{bf}} - 1\right)} \tag{2.2}$$

where in the limit of particle volume fractions much less than one, and base particle thermal conductivity much greater than that of the base fluid, Maxwell's theory predicts a linear dependence on particle loading. The resulting expression is known as the 3ϕ limit:

$$\frac{k_{eff,Max}}{k_{bf}} = 1 + \frac{3\phi_p\left(\frac{k_p}{k_{bf}} - 1\right)}{\left(\frac{k_p}{k_{bf}} + 2\right) - \phi_p\left(\frac{k_p}{k_{bf}} - 1\right)} \approx 1 + \frac{k_p(3\phi_p)}{k_p(1-\phi_p)} \approx 1 + 3\phi_p \tag{2.3}$$

2.2 Modified Effective Medium Theories

Although a few experimental studies report no anomalous thermal conductivity enhancement beyond the 3ϕ limit [31, 54, 55], some findings have demonstrated a nonlinear dependence on particle loading [13, 14], contrary to Maxwell's theory. Nanofluid thermal conductivity enhancement exhibiting strong size, shape, and temperature dependency have also been reported [56-58]. Modified EMTs considering a dependency on particle shape have been developed [39, 41], which predate anomalously reported findings.

Hamilton-Crosser (H-C) developed a new model for the effective thermal conductivity of heterogeneous mixtures [41]; derived without consideration of electrical conductivity, as Maxwell's theory had accomplished. Instead, H-C's model considers a two-phase heterogeneous system consisting of various shaped particles dispersed in either regular or irregular arrays within a base fluid. The thermal conductivity of this mixture is defined as:

$$k_{eff} = \frac{k_{bf}V_{bf}(dT/dx)_{bf} + k_pV_p(dT/dx)_p}{V_{bf}(dT/dx)_{bf} + V_p(dT/dx)_p} \tag{2.3}$$

where V is volume and (dT/dx) represents the overall average temperature gradients within the particles or base fluid. Based on the solution of Laplace's equation in spherical coordinates, Maxwell [24] determined the average temperature gradient ratio to be:

$$\frac{(dT/dx)_p}{(dT/dx)_{bf}} = \frac{3k_{bf}}{k_p + 2k_{bf}} \tag{2.4}$$

Referring to Maxwell's derivation, H-C determined a similar expression for this ratio:

$$\frac{(dT/dx)_p}{(dT/dx)_{bf}} = \frac{nk_{bf}}{k_p + (n-1)k_{bf}} \tag{2.5}$$

which incorporated an empirical shape factor or sphericity variable, *n*, given by:

$$n = \frac{3}{\Psi} \tag{2.6}$$

where Ψ is particle sphericity. Sphericity is defined as the ratio of the effective surface area of a sphere, equal in volume to that of the particle in suspension, to the surface area of the particle. In accordance with Maxwell's expression $n = 3$ for spherical particles. For cylindrical particles, $n = 6$. By applying Eq. 2.5 to Eq. 2.3, and dividing the numerator and denominator by total heterogeneous mixture volume, H-C theory provides the following expression for effective nanofluid thermal conductivity:

$$\frac{k_{eff,HC}}{k_{bf}} = \frac{k_p + k_{bf}(n-1) - \phi_p(k_{bf} - k_p)(n-1)}{k_p + k_{bf}(n-1) + \phi_p(k_{bf} - k_p)} \tag{2.7}$$

On the other hand, a modified EMT employing a theoretical approach more similar to Maxwell's methodology is the well-known Hashin-Shtrikman (H-S) bounds. [39, 40]. H-S derived upper and lower bounds for magnetic permeability in multi-phase composites, stating that they are analogous to bounds for effective thermal conductivity [59]. . In the case of $k_p >> k_{bf}$ and $\phi << 1$, the H-S lower bound represents Maxwell's EMT for well-dispersed spherical nanoparticles in a base fluid matrix,

$$\frac{k_{eff,HS,low}}{k_{bf}} = 1 + \frac{3\phi(k_p - k_{bf})}{3k_{bf} + (k_p - k_{bf})(1-\phi)} \tag{2.8}$$

Conversely, the H-S upper bound represents large volumes of particle-free base fluid separated by regions of chain-like or clustered nanoparticles [23].

$$\frac{k_{eff,HS,up}}{k_p} = 1 - \frac{3(1-\phi)(k_p - k_{bf})}{3k_{bf} - \phi(k_p - k_{bf})} \quad \textbf{(2.9)}$$

Equation 2.9 predicts theoretical conductivity enhancement due to preferential heat transfer through particle clusters. Although introduced in 1963, the H-S upper bound explains the mechanism only recently demonstrated to be the determining factor for thermal conductivity enhancement in nanofluids.

A relatively recent modified EMT considering high particle aspect ratio and thermal interface resistance, known as Kapitza resistance, was developed by Nan et al. [38, 42]. Nan et al.'s generalized model for effective nanofluid thermal conductivity is expressed as

$$\frac{k_{eff,Nan}}{k_{bf}} = \frac{3 + \phi[2\beta_{11}(1-L_{11}) + \beta_{33}(1-L_{33})]}{3 - \phi(2\beta_{11}L_{11} + \beta_{33}L_{33})} \quad (2.10a)$$

with constants L and β defined as

$$L_{11} = \frac{p^2}{2(p^2-1)} - \frac{p}{2(p^2-1)^{3/2}}\cosh^{-1}(p) \quad (2.10b)$$

$$L_{33} = 1 - 2L_{11} \quad (2.10c)$$

$$\beta_{ii} = \frac{k_{ii}^c - k_{bf}}{k_{bf} + L_{ii}(k_{ii}^c - k_{bf})} \quad (2.10d)$$

and *ii* subscripts referring to the principal axes of particles shaped as prolate ellipsoids, where

$$a_{11} = a_{22} < a_{33} \quad (2.10e)$$

The constants p and k^c are defined as

$$p = a_{33} / a_{11} \tag{2.10f}$$

$$k_{ii}^{c} = \frac{k_p}{1 + \gamma L_{ii}(k_p / k_{bf})} \tag{2.10g}$$

and lastly, γ is defined as

$$\gamma = \frac{(2 + 1/p) R_{bd} k_{bf}}{a_{11} / 2} \tag{2.10h}$$

where R_{bd} is the Kapitza resistance, which has been demonstrated from molecular dynamics simulations to be on the order of 10^{-8} m^2K/W [60]. As demonstrated in Fig. 2.1, the majority of reported nanofluid thermal conductivity enhancement is well-described by Nan et al.'s EMT and the HS bounds.

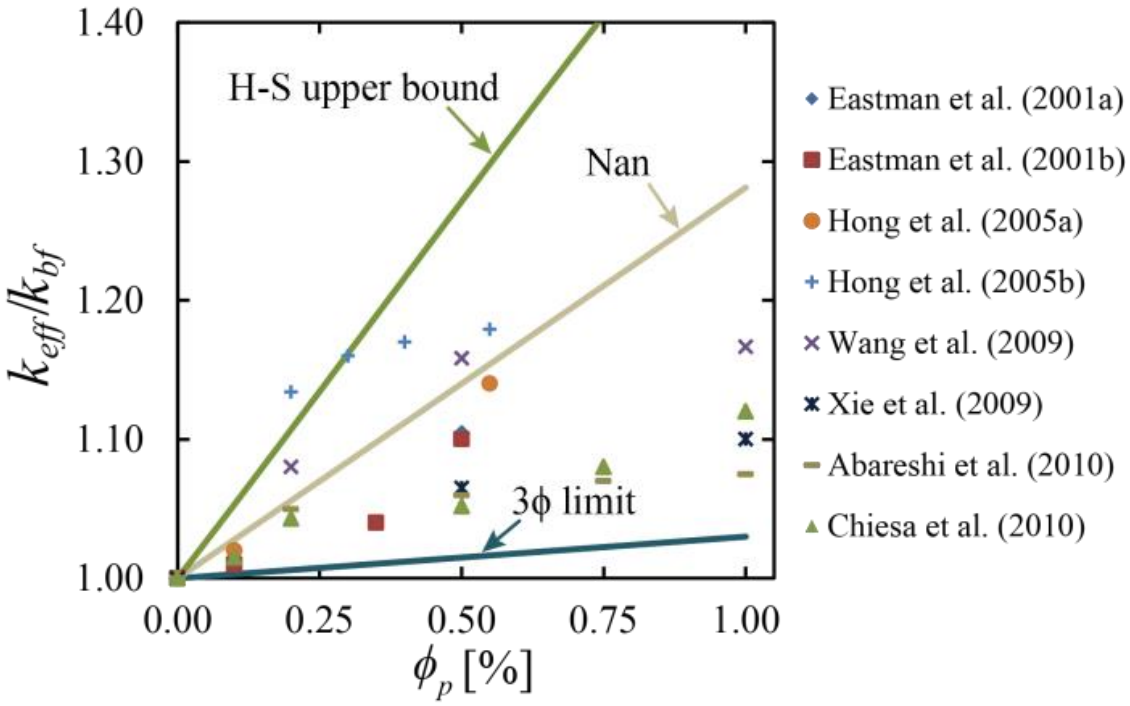

Fig. 2.1 Overview of reported normalized nanofluid thermal conductivity (k_{eff}/k_{bf}) [13, 14, 61-64]. The majority of literature values are well-bounded by Hashin-Shtrikman upper and lower limits [39], and Nan et al.'s EMT for high aspect ratio particles [38, 42].

2.3 Derivation of Nanofluid Thermophysical Properties

2.3.1 Nanofluid Density

Although nanofluid thermal conductivity requires mathematically intensive derivation, thermo-physical properties such as density and specific heat are traditionally derived from conservation of mass and energy. Nanofluid density is the simplest of these derivations. Starting with conservation of mass,

$$m_{nf} = \sum_i m_i \tag{2.11}$$

where subscript *nf* signifies nanofluid, Eq. 2.11 can be re-written expressing mass as the product of density and volume to describe a binary mixture of nanoparticles and base fluid.

$$(\rho V)_{nf} = (\rho V)_{bf} + (\rho V)_p \tag{2.12}$$

Dividing both sides by nanofluid volume, V_{nf}, creates volume ratios of base fluid and nanoparticle volume over total nanofluid volume.

$$\rho_{nf} = \rho_{bf} \frac{V_{bf}}{V_{nf}} + \rho_p \frac{V_p}{V_{nf}} \tag{2.13}$$

Since volume fraction is defined as the volume of a constituent material divided by the total volume of all constituent materials in a mixture,

$$\phi_i = \frac{V_i}{V_{total}} \tag{2.14}$$

and the sum of all volume fractions in a mixture is equal to one,

$$\sum_i \phi_i = 1 \tag{2.15}$$

Eq. 2.13 can be simplified to give the following expression for effective nanofluid density:

$$\rho_{nf} = \rho_{bf}(1-\phi_p) + \rho_p \phi_p \tag{2.16}$$

Nanofluid density is expected to linearly increase with particle addition, though this effect is fairly negligible (1.3 % increase in density for a 1 % increase particle volume fraction).

2.3.2 Nanofluid Specific Heat

Nanofluid specific heat is derived from conservation of energy,

$$(mC_p\Delta T)_{nf} = (mC_p\Delta T)_{bf} + (mC_p\Delta T)_p \tag{2.17}$$

assuming that the temperature change of the nanoparticles and base fluid are equivalent to the temperature change of the nanofluid. Thus, eliminating ΔT and expressing mass as the product of density and volume produces the following expression:

$$(\rho VC_p)_{nf} = (\rho VC_p)_{bf} + (\rho VC_p)_p \tag{2.18}$$

Again, dividing both sides by nanofluid volume produces volume ratios that may be simplified into volume fractions. Finally, by dividing both sides by nanofluid density, expressed in the form of Eq. 2.16, effective specific heat is defined as:

$$C_{p,nf} = \frac{(\rho C_p)_{bf}(1-\phi_p) + (\rho C_p)_p\phi_p}{\rho_{bf}(1-\phi_p) + \rho_p\phi_p} \tag{2.19}$$

When the product of density and specific heat of the base fluid is larger than that of the particle, nanofluid specific heat is expected to linearly decrease with particle addition. As mentioned previously, this prediction is inconsistent with recent experimental findings [44, 45], which claim that semi-solid layers formed at particle interfaces support enhanced heat capacity.

2.3.3 Nanofluid Thermal Diffusivity

Traditionally, thermal diffusivity is defined as thermal conductivity divided by the product of density and specific heat. Thus, nanofluid thermal diffusivity can be simply described by the following equation:

$$\alpha_{nf} = \left(\frac{k}{\rho c_p} \right)_{nf} \tag{2.20}$$

Since specific heat capacity is expected to decrease with particle addition, and density exhibits a negligible increase with particle addition, EMT predicts an increase in nanofluid thermal diffusivity similar to that of thermal conductivity.

2.3.4 Nanofluid Latent Heat of Fusion

Latent heat of fusion is a mass specific property, defined as the amount of energy required to change a material from solid to liquid phase at a constant temperature. Nanofluid latent heat of fusion is described by the material within the nanofluid contributing to phase change. Since nanoparticles suspended in a base fluid do not change phase at the base fluid melting temperature, nanofluid latent heat of fusion is expressed as the product of base fluid mass fraction and latent heat of fusion:

$$h_{sl,nf} = (h_{sl} w_p)_{bf} \tag{2.21}$$

Weight percent can be replaced with an equivalent function of particle volume fraction through the following relationship:

$$w_{bf} = \frac{m_{bf}}{m_{nf}} = \frac{\rho_{bf}}{\rho_{nf}} \left(\frac{V_{bf}}{V_{nf}} \right) = \frac{\rho_{bf}}{\rho_{nf}} (1 - \phi_p) \tag{2.22}$$

By substituting Eqs. 2.16 and 2.22 into Eq. 2.21, nanofluid latent heat of fusion can be defined as a function of particle volume fraction.

$$h_{sl,nf} = \frac{\rho_{bf} h_{sl,bf} (1 - \phi_p)}{\rho_{bf} (1 - \phi_p) + \rho_p \phi_p} \tag{2.23}$$

Nanofluid latent heat of fusion is expected to linearly decrease with particle addition, as the mass fraction of base fluid is reduced. Therefore, nanofluid latent heat of fusion, as defined in Eq. 2.23, is hereafter referred to as the mass loss prediction.

Chapter 3

Sample Fabrication and Characterization

Nanofluids consist of two parts: base fluid and nanoparticles. Although paraffin wax was chosen as a base fluid for its high specific storage capacity, melting temperature is equally important depending on the intended application. Paraffin wax is composed of hydrocarbon molecules of the form C_nH_{2n+2}, which are either arranged in straight chains (normal or n-paraffin) or branched chains (isoparaffin). Density and melting point is dependent on the number of carbon atoms in the hydrocarbon chain, *n*, which range between 20 and 40 for paraffins. Since domestic hot water is typically provided at 50 °C, paraffin PCM with a similar melting temperature may be selected to minimize inefficiency due to excess parasitic heat loss to ambient. Paraffin wax (126 MP Wax - 3032, Candlewic) with a melting temperature of ~53 °C was purchased for this characterization study.

There are several physical properties of nanoparticles to consider for favorable thermal storage performance. To avoid precipitation, it is ideal to use a material with counteracting body forces (gravity and buoyancy). In addition, nanoparticle geometry plays a significant role in thermal conductivity enhancement, as traditional effective medium theory only applies for perfectly spherical particles. Nan's modified effective medium theory indicates that high aspect ratios are desirable for greater thermal conductivity enhancement. Due to their preferable shape and physical properties, MWNTs were chosen for the paraffin-based suspensions investigated in our characterization study of nanofluid thermal properties.

This chapter presents the sample preparation procedure used to fabricate our nanofluid samples, and the characterization methods applied to measure their thermal properties. Detailed procedure for subsequent density measurements, stability testing, and imaging of the fabricated samples are provided, along with any observations made. Also included is an overview describing the operating principles and development of our measurement technique for both differential scanning calorimetry and laser flash analysis testing. Lastly, suggestions for potential refinements in measurement technique are explained, for the purpose of future study.

3.1 Nanofluid Sample Preparation

MWNTs (Cheap Tubes Inc.) of 15.5, 40, 65, and 400 nm outer diameters were dispersed into paraffin wax with high frequency pulse sonication (VCX750 Ultrasonic Processor, Sonics & Materials, Inc.). Ultrasonication is a typical method for dispersing highly aggregated nanoparticles [65, 66].= Stock nanofluids of 0.2, 0.5, and 1.0 % volume fraction were prepared for each MWNT diameter, producing a total of twelve stock mixtures.

As described in Section 2.3.4, nanoparticle mass fraction can be expressed as the ratio of nanoparticle density to nanofluid density, multiplied by nanoparticle volume fraction. Per conservation of mass, nanofluid mass is equivalent to the sum of nanoparticle and base fluid masses. Hence, an expression for nanoparticle mass as a function of particle volume fraction and base fluid mass is obtained.

$$m_p = \left[\frac{\rho_p \phi_p}{\rho_{bf}(1-\phi_p)} \right] m_{bf} \tag{3.1}$$

An arbitrary mass of base fluid was weighed on a precision balance (Explorer Pro, OHAUS), with a resolution of 0.1 mg. Corresponding nanoparticle weight for each desired volume fraction, given by Eq. 3.1, was measured and added to liquid wax heated to 85 °C on a hot plate (Isotemp, Fisher Scientific). Stock mixtures were sonicated at a frequency of 20 kHz and output power of 750 W for on/off pulses of 25/10 seconds, until achieving one hour of active sonication time. A stock of pure paraffin was also sonicated, as a control, in furtherance of consistent sample preparation. Figure 3.1 illustrates how stock nanosuspensions were sonicated in the arrangement described.

Fig. 3.1 Photograph of stock ultrasonication procedure. The ultrasonicator probe is inserted into a vial of unmixed nanofluid stock placed on a hot plate.

Once mixed, stock nanosuspensions were poured into an acrylic mold, solidified, and cut into 12x12 mm squares with a precision blade – one sample at a time. To eliminate uncertainty in fabrication conditions within a batch of samples from the same stock,

samples were fabricated continuously until the stock was completely depleted. Since the orientation of particles in suspension may possibly change during melting/solidification cycles, each batch was prepared immediately after sonication and stock mixtures were maintained in liquid state for the duration of the fabrication process. Excess material from the cutting process or from botched samples was discarded, not re-melted and re-molded. An aluminum rod was lightly pressed into the mold to mitigate void formation during solidification. Figure 3.2 shows a photograph of a fabricated nanofluid sample and sonicated paraffin control sample.

Fig. 3.2 Image of a prepared sonicated pure paraffin sample and a 15.5 nm diameter, 0.2 % volume fraction nanofluid sample.

Samples were given identification codes based on the following system: SPNSAAA_BBB_CD. AAA corresponds to particle volume fraction, given as 002 for 0.2 %, etc. SPNS stands for sonicated paraffin nanosuspension. BBB represents particle diameter, given as 065 for 65 nm particles, etc. C indicates the type of testing to be performed: 1 is latent heat of fusion measurement with DSC; 2 is specific heat measurement with DSC; 3 is solid sample LFA; 4 is liquid sample LFA. Finally, D states the test number for that sample and test type. For example, the sample ID for the third nanofluid sample of 400 nm diameter particles at 1 % volume fraction, tested in the LFA at solid state, is SPNS400_010_33.

3.2 Sample Density Determination

Individual sample density was measured with an Archimedes kit (OHAUS), shown in Fig. 3.3, to assure consistency with effective medium theory. Archimedes' principle states that the buoyancy force exerted on an immersed object is equal to the weight of fluid displaced by the object. Distilled water was used as the auxiliary liquid, with a measured temperature of 22 °C. Since paraffin is less dense than water, a holder for floating solids was suspended from the bracket above the glass beaker. The balance was initially tared and the weight of a sample in air was measured in either of the two weighing pans at the base of the scale. The sample was submerged in the auxiliary fluid and positioned under the suspended holder, assuring that no bubbles had adhered to the sample surface.

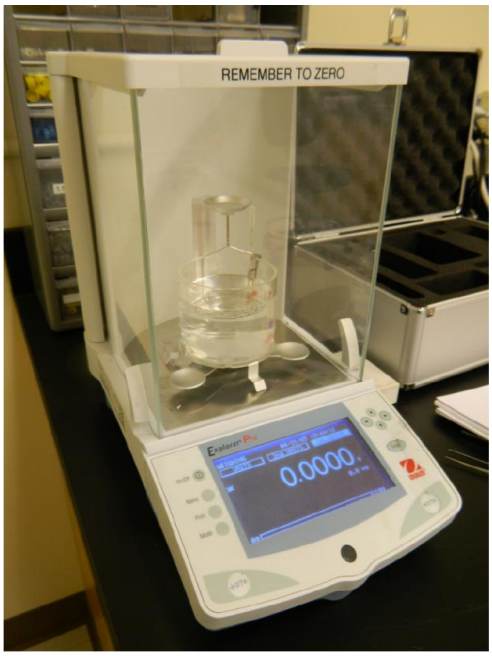

Fig. 3.3 Precision balance equipped with an Archimedes kit to determine the density of solid nanofluid samples.

The weight of the displaced fluid, which exerts an upward force on the scale and produces a negative reading, was recorded. The following equation was used to determine sample density:

$$\rho_{nf} = \frac{w_a}{w_a - w_f}(\rho_f - \rho_a) + \rho_a \tag{3.2}$$

where w is the weight of the sample, measured in a medium denoted by subscripts a and f for air and fluid, respectively. At 22 °C, the density of air is approximately 1.2 kg/m^3, and the density of water is 997.8 kg/m^3. At least six samples were prepared from each stock, and each sample was measured at least five times to check repeatability. The resulting values for each MWNT diameter, compared to the theoretical nanofluid density, can be seen in Figs. 3.4 (a)-(d).

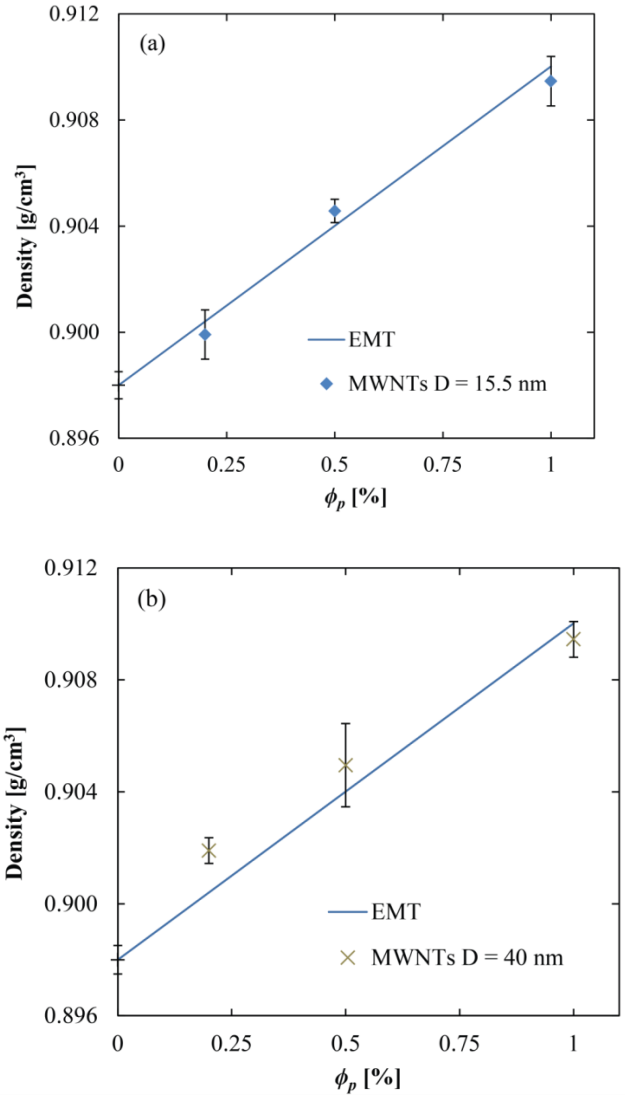

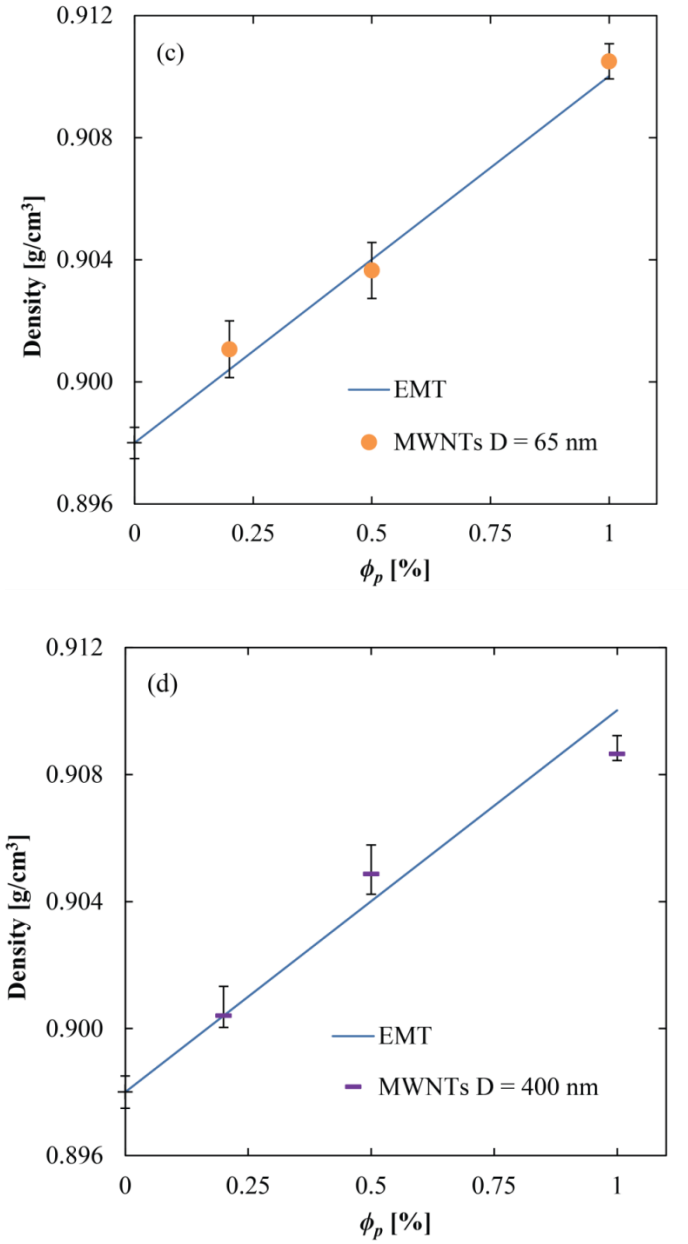

Fig. 3.4 Measured density of nanofluid samples with various diameter MWNTs, (a) 15.5 nm (b) 40 nm (c) 65 nm (d) 400 nm. All measured sample densities are compared to the respective theoretical nanofluid density defined by EMT.

Density values within a single volume fraction had a maximum standard deviation of 2.70 kg/m^3 (0.30 %), and all samples followed effective medium theory with a root mean square error of 1.57 kg/m^3.

3.3 Nanofluid Stability Testing

Suspension stability was examined with an optical microscope (SMZ1500, Nikon), since paraffin generates surface charge accumulation that impedes imaging with electron microscopy (Fig 3.5).

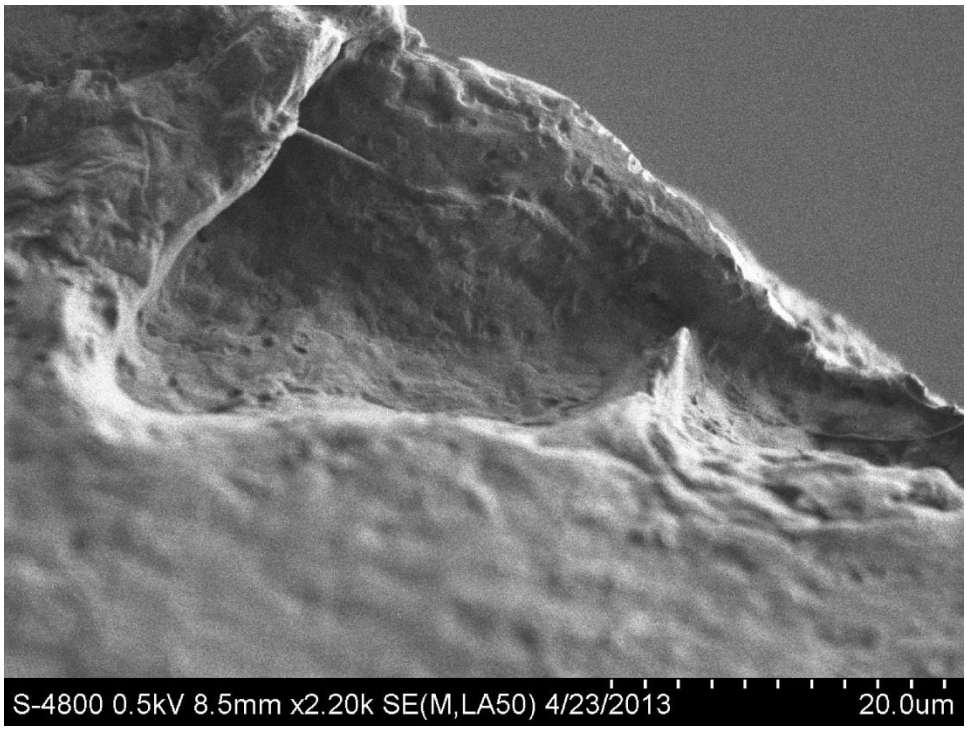

Fig. 3.5 SEM image of 15.5 nm MWNT diameter nanofluid sample with the following imaging conditions: 0.5 kV acceleration voltage, 2μA load current, and a 31 degree lateral stage tilt. Paraffin's electrically insulating properties prevent imaging of suspended nanoparticles within the base medium.

Samples were imaged before and after latent heat characterization, to examine effects of melt cycling on particle cluster formation. Although the samples imaged exhibited significant particle aggregation, no discernible change in the degree of aggregation was observed after melt cycling (Figs. 3.6 (a) and (b)). The optical microscope used was not equipped with a reticule to measure a precise scale bar. Thus, an approximate scale bar was acquired by capturing two identical images of a sample, with and without an overlaid

27 gauge hypodermic needle. Although imprecise, both images were taken at the same magnification, and the approximated scale bar is included as a reference.

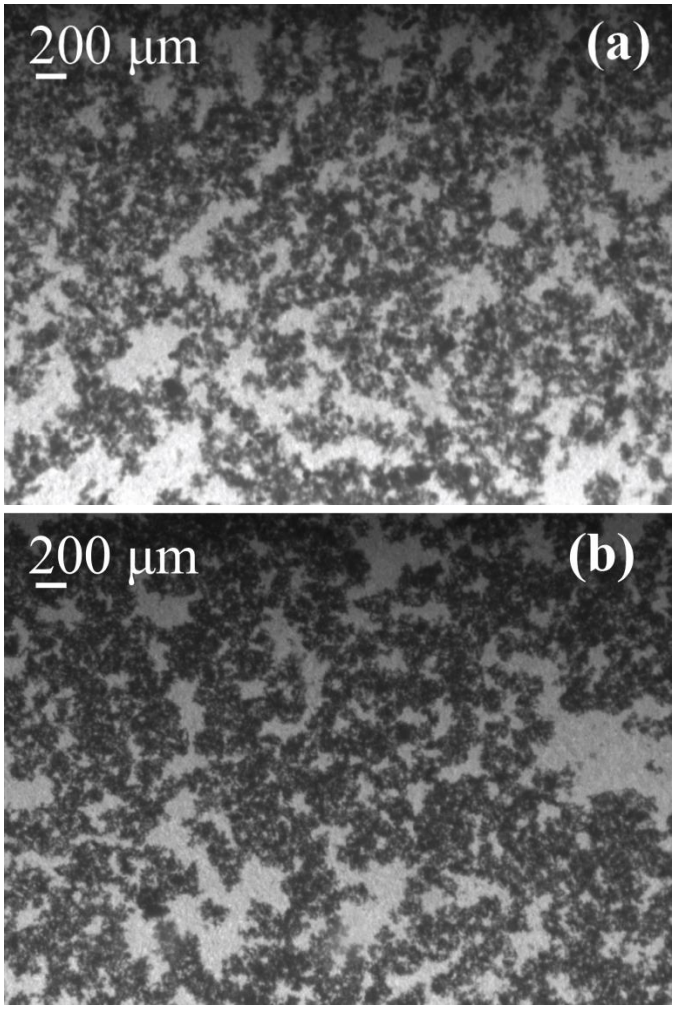

Fig. 3.6 Optical microscope images of 0.2 % volume fraction, 15.5 nm diameter MWNTs/paraffin nanofluids. (a) Image taken after fabrication. (b) Image taken after melt cycling.

Additional stability testing was conducted by observing stock suspensions either continuously left in liquid state on a hot plate, or run through multiple melting cycles. The melt-cycled stock underwent two melts per day and was maintained in liquid state for two hours per melt. Over a five day period, both stock suspensions tested showed no visible signs of sedimentation, as demonstrated in Fig. 3.7.

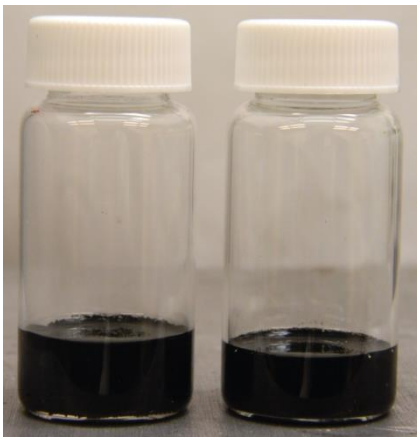

Fig. 3.7 Nanofluid stock used in stability testing. The left vial contains stock continuously left in liquid state for five days. The right vial contains stock after five days of melt cycling, where melted twice per day and maintained in liquid state for two hours per melt. No precipitation was observed in either test.

3.4 Differential Scanning Calorimetry Testing

3.4.1 Technique and Sample Preparation

Sample latent heat of fusion was measured utilizing differential scanning calorimetry (DSC) (NETZSCH STA 449 F3 Jupiter), with 1 μV/mW sensitivity and ±3 % measurement uncertainty. A schematic of the instrument used is shown in Fig. 3.8.

DSC involves the measured difference in input heat flux per unit mass required to maintain the temperatures of an empty reference crucible and sample crucible at a set heating rate, in a temperature controlled furnace. This specific input heat flux is recorded as DSC signal [W/g]. During melting, a large amount of input heat flux is required to overcome sample latent heat. This endothermic reaction corresponds to a peak in the DSC signal with respect to temperature, beginning at the melting temperature of the material. A sample's latent heat of fusion is measured as the area under the DSC melting peak. The positioning of the sample carrier and the orientation of the sample and reference crucibles are illustrated in Fig. 3.9.

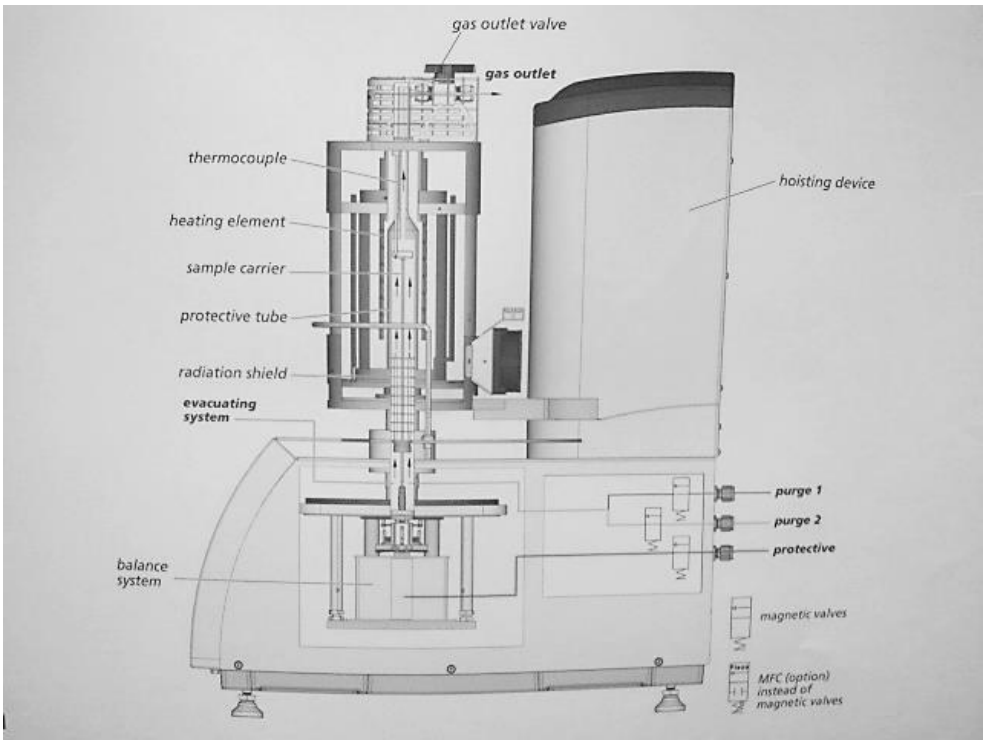

Fig. 3.8 Inner Schematic of the NETZSCH STA 449 F3 Jupiter. Courtesy NETZSCH Instruments.

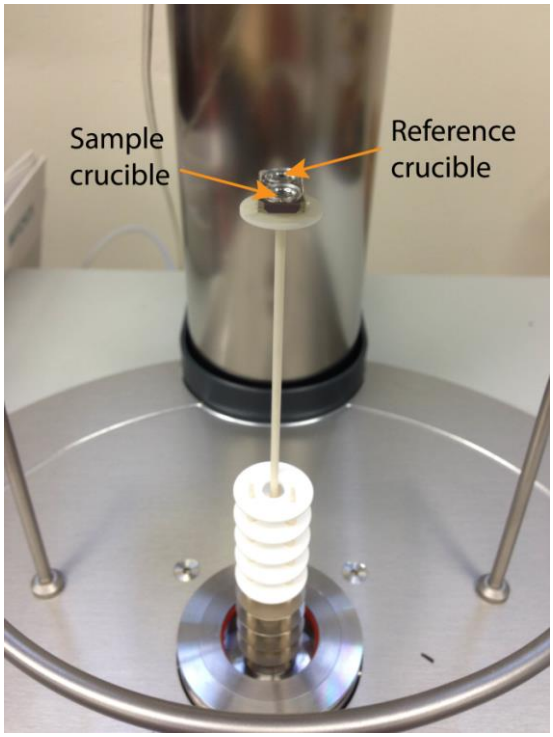

Fig. 3.9 Photograph of the DSC sample carrier, holding the reference crucible (back) and sample crucible (front).

The accuracy of DSC onset temperature [K] and latent heat of fusion [J/g] measurements are affected by furnace heating rate [K/min]. The sample carrier/measurement sensor has low sensitivity with respect to temperature at fast temperature rates (10-20 K/min). Thus, measurements intended to accurately measure melting/crystallization onset should be taken at low temperature rates (1-5 K/min) to ensure high sensor sensitivity with respect to temperature. Latent heat measurements, on the other hand, are more dependent on energy than temperature.

For DSC measurements, an initial baseline or correction test is required to measure empty system conditions over the duration of a set temperature program. Measured fluctuations in the empty system are assumed to be recurrent during the subsequent sample measurement, and are subtracted from sample measurement results. Baseline measurements are taken with two empty crucibles. Since DSC is a sensitive, mass specific measurement, the crucible bases and lids were weighed to ensure each set are of equivalent mass. After baseline measurement, the same temperature program is re-run upon placing a sample in the sample crucible. During sample placement, caution was taken not to disrupt the sample carrier or the position of the reference crucible in the sample holder. Additionally, since the sample crucible was removed from the holder for sample placement, a marking had been made on the crucible side and lid to return it to its original position in the holder. These precautions were taken for all baseline and sample measurements. Any small changes in positioning of the crucibles or sample holder can considerably impact DSC signal.

Sample contact area on the base of the crucible also influences DSC signal. To achieve repeatable measurements, sample contact area should not change between melt

cycles. Therefore, it is suggested to neglect first melt cycle data as the sample undergoes its initial melt and conforms to the crucible base. Since paraffin's melting temperature is relatively low, and can be quickly melted on a hot plate, samples were pre-melted in the crucible to minimize change in contact area during testing. For this characterization study, however, first melt cycle data was discarded to avoid any potential uncertainty due to contact area.

3.4.2 Development of DSC Temperature Program

3.4.2.1 Sample Mass

A temperature program was developed to run nanofluid samples through three consecutive melting/solidification cycles. Refinement of temperature program parameters such as heating/cooling rate, isothermal period duration, and set melting time was conducted to ensure measurement accuracy and reliability. Initially, it was unknown if sample mass affected DSC measurement. In order to eliminate this potential uncertainty, measurements of pure sonicated wax were run with variable masses, ranging from 2.5 to 10.0 mg.

As shown in Fig. 3.10, sample mass does significantly affect DSC signal. The lowest sample mass, 2.5 mg, generates a highly disjointed curve with significant noise, which introduces error in calculation of the area under the curve used to calculate latent heat of fusion. Samples of greater mass appear to generate much less signal noise, with the 10.0 mg sample producing the most stable curve. Paraffin samples larger than 10.0 mg were not attempted because the sample crucible could not accommodate a greater volume. Therefore, to ensure clean signal and avoid uncertainty due to sample mass, all measured nanofluid samples were cut and weighed to precisely 10.0 mg prior to testing.

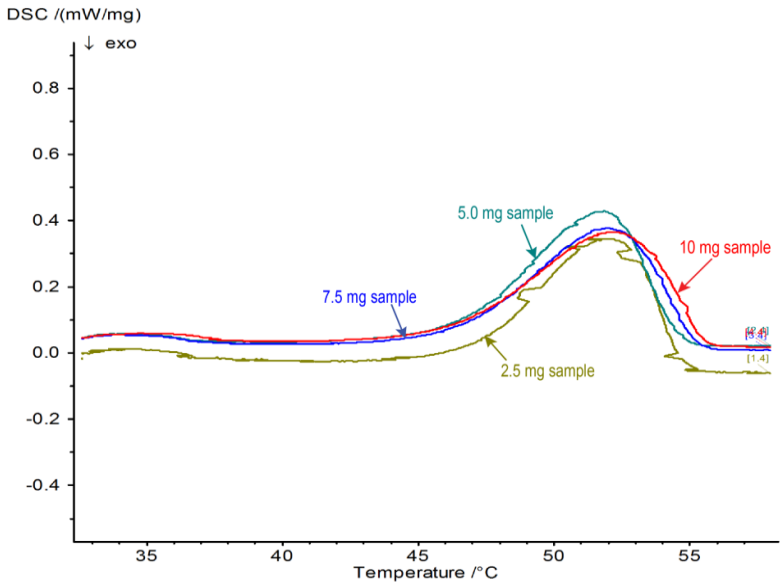

Fig. 3.10 Measured DSC with respect to temperature for 2.5, 5, 7.5, and 10.0 mg sonicated wax samples, run with the same baseline measurement and 1 K/min temperature program. The DSC signal becomes less noisy as sample mass is increased.

3.4.2.2 Heating/Cooling Rate

Since DSC measures heat flux differential between reference and sample, higher heat fluxes are desirable to give a clearer indication of this difference. For example, at a heating rate of 1 K/min, a sample will only require the amount of energy specified by its specific heat to rise one degree Kelvin in one minute. Comparing this to the heat transferred in an empty reference crucible by natural convection in one minute, the difference in input energy may not be significant; especially considering a sample with low specific heat. Conversely, to match the temperature rise of the reference crucible at higher heat rates, larger input heat fluxes are needed to overcome sample sensible heat energy requirements. Hence, faster heating rates will generate greater input heat flux differentials between reference and sample. This discrepancy is illustrated in Fig. 3.11, where although similar latent heats of fusion (h_{sl}) are calculated from the areas under both curves, the 5 K/min ramp rate produces a sharper and much more well-defined phase change curve –

with a peak input heat flux about 3.5 times greater than the 1 K/min curve. It is also noted that the 5 K/min phase change curve shows a more visible initial solid-solid phase change prior to melting, indicated by the lower endothermic peak in DSC signal. This solid-solid phase transition is common in paraffins, and is explained by the loss of fixed orientation of atoms and molecules in the structure during heating [67, 68].

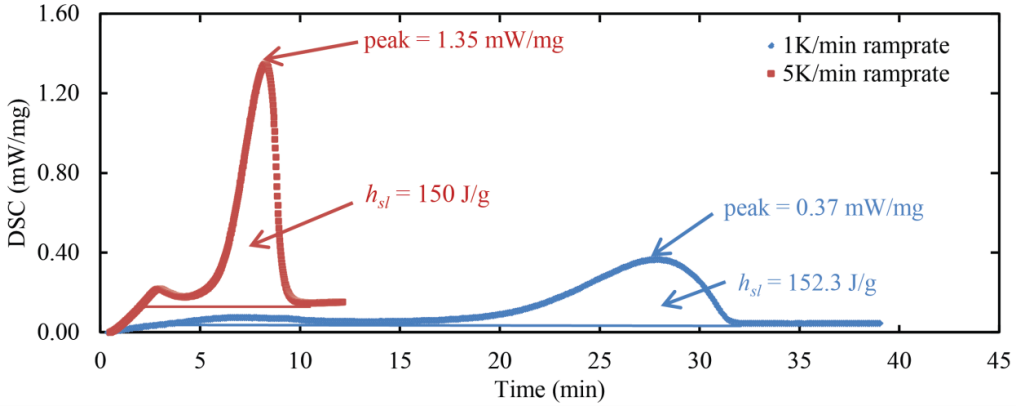

Fig. 3.11 DSC curves for sonicated pure paraffin at a 1 K/min ramp rate and 5 K/min ramp rate. The 5 K/min ramp rate produces a clearer phase change curve with a significantly higher input heat flux.

10 K/min and 20 K/min heating rates also increase input heat flux to the sample; however, there is a productivity limitation with using these higher ramp rates. At higher rates, the peak set temperature must be set well beyond melting temperature to ensure enough time for melt. For example, at 20 K/min, if 10 mg of paraffin requires 1.5 J to fully melt and receives an average input DSC of 2.5 mW, it will take 10 minutes to change phase, producing a 200 K temperature rise. Without controlled cooling, the furnace cannot return to room temperature from these elevated temperatures during the allotted cool down period, even at a 1 K/min cooling rate. Actually, the furnace does not cool at the specified cooling rate. Instead, the DSC software defines a set duration for the cooling period based on inputted start temperature, final temperature, and cooling rate. Therefore, an extra

isothermal period is typically needed to stabilize DSC signal and furnace temperature near room temperature to initiate the next melt cycle. To shorten the duration of the required isothermal period, cool down must begin at relatively lower peak furnace temperatures, which is achieved by lowering heating rate. In addition, the sample does not fully crystallize during the cooling period. The DSC software does not record data from isothermal periods, where a significant portion of crystallization occurs. Therefore, the latent heat of crystallization was not measured. A temperature-controlled furnace with liquid nitrogen cooling is needed to achieve full crystallization during the cooling period.

The development of an appropriate temperature program was an iterative process, conducted by testing parameters such as heating and cooling rate, peak furnace temperature, melting duration, and end cycle temperature. The parameters for each temperature program tested are detailed in Table 3.1. Ramp rates 1 and 2, for example, did not allow enough time to melt the sample, and could not cool to the sufficient end cycle temperature due to their high cooling rates. Therefore, cooling periods were set to reach 0 °C at 1 K/min to achieve the longest possible cooling duration, and reach end cycle temperatures below paraffin's solid-solid phase transition temperature (~34 °C). 5 K/min heating and 1 K/min cooling rates were shown to produce sufficient melt time, but did not return samples to an adequate end cycle temperature. Further reduction of end cycle temperature requires longer isothermal times after cooling. This additional analysis is detailed in the following section.

Table 3.1 DSC melt cycle parameters used to develop an appropriate temperature program. Ramprate6 was chosen as the optimal temperature program for the nanofluid characterization study.

Temperature program	Test time [hrs]	Heating rate [K/min]	Cooling rate [K/min]	Peak temperature set [°C]	Peak reached [°C]	Melt time set [min]	Melt time measured [min]	End cycle temperature [°C]
ramprate1	6.5	20	20	123	70.0	5	10	80.0
ramprate2	6.8	20	5	143	90.0	6	10	74.8
ramprate3	7.0	1	1	72	62.5	50	50	41.8
ramprate4	6.2	5	1	94	72.8	14	8	37.1
ramprate5	6.6	5	1	94	72.5	14	8	37.0
ramprate6	7.8	5	1	114	90.9	18	8	37.4

With 5 K/min and 1 K/min heating/cooling rates, the rest of the melt cycle parameters were fine-tuned to achieve stable post-melt DSC signal, prior to the start of cooling. Stable DSC signal at the end of a melting curve indicates that samples have fully melted. Based on measurement results, with an average input heat flux of 3.125 W/g, and 1.5 J required to melt, the necessary melting time for a 10 mg sample heated at 5 K/min is 8 minutes. Starting at 24°C, a sample would require a 50 K temperature difference to melt for 10 min at 5 K/min. Previous tests at a 5 K/min ramp rate had produced a roughly 20 K difference between set peak and peak reached, meaning the set peak should be set 20 °C higher to achieve true desired set peak. Therefore, the peak set for ramprate4 and ramprate5 was 94 °C. For ramprate6, the peak was set to 114 °C, to guarantee stabilized DSC signal post-melt, and to ensure that melting curves for nanofluid samples would not be truncated, due to possible melting curve shape variability with nanoparticle addition. The 20 K increase in set peak appeared to not affect end cycle temperature significantly.

3.4.2.3 Isothermal Period Duration

The final consideration for the developed temperature program was isothermal period length. Paraffin wax begins a solid-solid phase transition at roughly 34 °C. With reached cooling temperatures around 37 °C for ramprate6, the furnace requires at least an additional 3 K of cooling during an isothermal period to reach a suitable end cycle temperature (< 34 °C), and to allow for a period of stability in DSC signal at the start of the next heating cycle. As seen in Fig. 3.12, a 30-minute isothermal period separating melt cycles in ramperate6 ensures that not only has an appropriate temperature been reached before ramping up again (32.4 °C), but the DSC signal is stabilized for nearly 6 minutes between the start of heating and the initiation of phase change. With two additional 30-minute isothermal periods, the total test duration for ramprate6 is 8 hours and 46 minutes, allowing for two tests to be run per day.

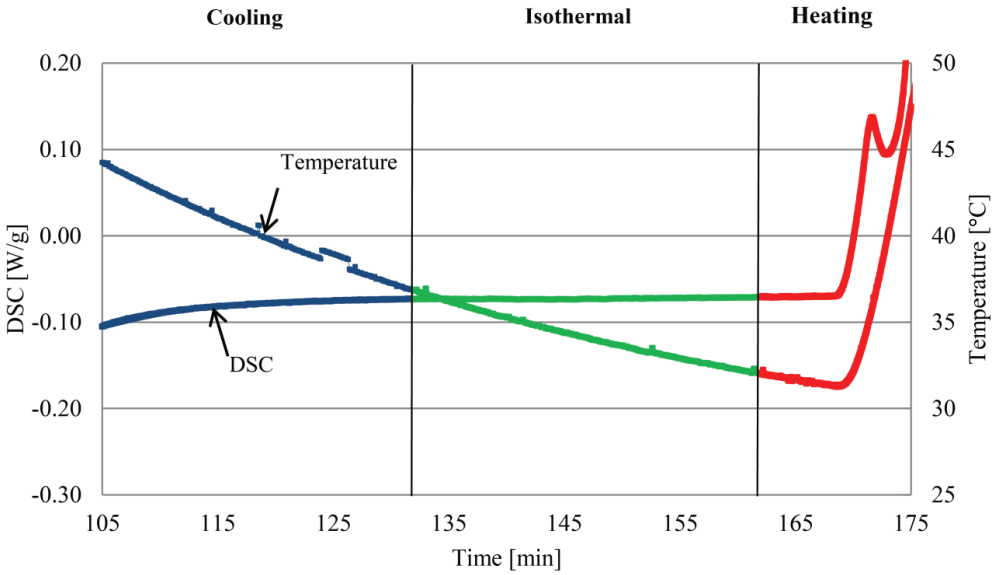

Fig. 3.12 Ramprate6 temperature program DSC signal and temperature with respect to time, depicting a paraffin DSC measurement's cooling, isothermal, and heating segments (separated by dashed vertical lines from left to right, respectively). Ramprate6 demonstrates stable DSC signals between melt cycles, and achieves adequate end cycle temperature below 34 °C.

The final version of the ramprate6 temperature program, developed for DSC latent heat of fusion characterization, is described in Fig. 3.13.

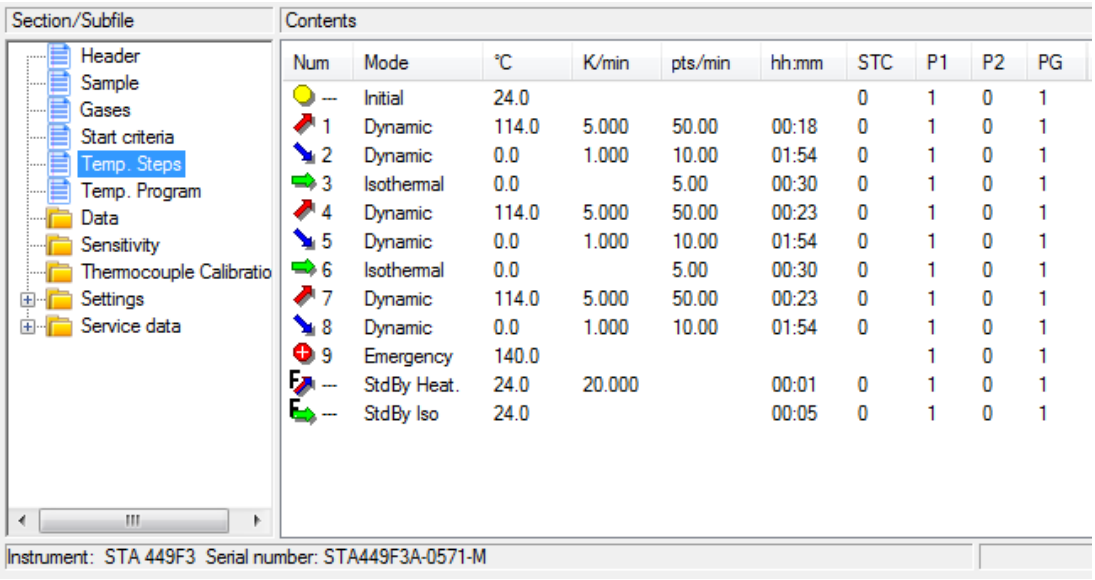

Fig. 3.13 Detailed steps for the ramprate6 temperature program used to conduct nanofluid latent heat of fusion characterization testing.

3.4.2.4 Baseline Reliability

With a temperature program set, the next consideration was reliability of measurement. DSC requires a baseline measurement to be run with an empty crucible in order to tare the instrument throughout the course of a set temperature program. With this technique, it is important to quantify how many consecutive samples can be run with the same baseline measurement. If the baseline DSC signal does not change significantly through the course of several measurements, more samples can be run in between baseline tests without affecting accuracy. In order to test for significant difference in baseline measurements over time, a new baseline was run every day, using the same temperature program, with one sample ran in between.

Three sets of 1 K/min baseline measurements were compared. As seen in Fig. 3.14, the baseline DSC measurements show increased divergence from day to day, up to a ±0.10

mW variability from baseline test 2 to 3. However, this change is negligible compared to the peak DSC measured during a sample measurement.

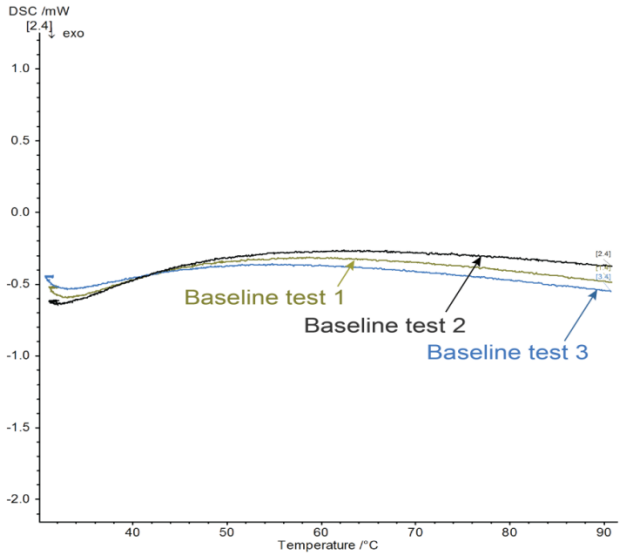

Fig. 3.14 Measured DSC vs. temperature for three 1 K/min baseline measurements, run on consecutive days, with sample measurements in between. The difference in observed DSC demonstrates developing variability over time as the instrument's empty system behavior changes with each measurement.

Looking back to Fig. 3.11, in which a 1 K/min ramp produced a peak heat flux of 0.37 mW/mg, or 3.7 mW with a 10 mg sample, a baseline variability of ±0.10 mW amounts to a ±2.70 % baseline uncertainty. Baseline uncertainty is negligible when it is less than the instrument uncertainty (±3.00 %). Hence, multiple consecutive samples may be run under the same correction file. With faster ramp rates, the baseline variability and peak DSC is expected to increase, as a result of higher magnitudes of input heat flux to the sample. To determine the effect of higher ramp rates on baseline uncertainty, the baseline variability of 5 and 10 K/min ramp rates were also tested by the same method as the 1 K/min baseline test. Resulting measurements for all ramp rates tested are compiled in Table 3.2. For a 5 K/min ramp rate, using the 1.35 mW/mg peak DSC (13.5 mW with a 10 mg sample) in Fig 3.11, and a baseline variability of ±0.40 mW after three measurements, the resulting

baseline uncertainty was ±2.97 %. Similarly, a 10 K/min ramp rate demonstrated a baseline uncertainty of ±2.64 %. The baseline variability for a 20 K/min ramp rate was not measured because a favorable temperature program could not be developed at that rate. Although each ramp rate tested showed a negligible baseline uncertainty after three sets of measurements, a fourth measurement increased baseline uncertainty beyond the ±3 % limit. Therefore, no more than three consecutive samples were run between baseline measurements for the latent heat characterization study.

Table 3.2 Baseline uncertainty in several DSC ramp rates, after three consecutive tests run with the same baseline. Baseline variability and peak DSC are shown to scale with ramp rate, producing similar baseline uncertainty among all ramp rates tested.

Ramp rate	Peak DSC (mW/mg)	Sample mass (mg)	Peak heat flux (mW)	Baseline variability (± mW)	Baseline uncertainty (± %)
1 K/min	0.37	10	3.70	0.10	2.70
5 K/min	1.35	10	13.50	0.40	2.97
10 K/min	2.00	10	20.04	0.53	2.64
20 K/min	3.21	10	32.12	-	-

3.4.3 Specific heat measurement

The STA 449 is also capable of specific heat measurements, employing similar techniques to those used for latent heat measurements. A sample and a reference crucible are run through a pre-determined temperature program, heating the sample through a desired temperature range. Specific heat measurements require three measurements: baseline, standard, and sample. A complete series of measurements must be carried out in immediate succession, using the same crucibles for each test. The standard – sapphire for this study – is a material of known specific heat with respect to temperature. To begin,

multiple baseline measurements are taken to ensure absolute consistency in empty system conditions. Typically, two or three consecutive baselines are run until baseline DSC signal shows nearly exact repeatability. This precaution is necessary because the DSC calculates specific heat according to a function of sample and standard DSC signals, corrected by baseline DSC signal (Eq. 3.3). Any deviation in the baseline measurement results in a significant loss in accuracy.

$$C_{p,sample} = \frac{m_{std}}{m_{sample}} \left(\frac{DSC_{sample} - DSC_{Base}}{DSC_{std} - DSC_{Base}} \right) C_{p,std} \tag{3.3}$$

Once a repeatable baseline is established, the sapphire standard is run, with the same temperature program as the baseline. It is suggested to run a standard with similar mass to the eventual sample to be tested, in order to produce a similar magnitude DSC signal as the sample run. The sapphire standard may also be run multiple times to assure the measurements are reproducible. Lastly, the sample measurement is run with the same temperature program as the baseline and standard. Measurement of an additional sample may be conducted immediately following the first, but the entire measurement process should be repeated for each sample to ensure accuracy.

3.4.3.1 Validity of Paraffin Specific Heat Measurements

An appropriate temperature program for specific heat requires a stable initial furnace temperature. Since ambient temperature fluctuations may lead to unstable furnace temperatures near room temperature, the initial temperature was set to 30 °C. An isothermal period of 15 minutes was set to equalize furnace temperature prior to the heating phase. Although the set initial temperature is below the onset temperature of paraffin (34 °C), it does not provide an adequate amount of time for the DSC signal to stabilize prior to

melting. Unfortunately, specific heat measurements cannot incorporate DSC signal recorded during phase change. Thus, without controlled cooling, the DSC is incapable of taking accurate specific heat measurements of paraffin in solid state. On the other hand, liquid phase specific heat measurement is possible, but requires much longer test durations for samples to cool from higher temperatures. Since specific heat measurements must be taken in immediate succession, a complete set of testing for a single sample is impractically long, and was not attempted. Thus, the procedure for specific heat measurements has been outlined in this section, but no measurement results are reported in the following chapter.

3.5 Laser Flash Analysis

Nanofluid thermal diffusivity was measured utilizing laser flash analysis (LFA) (NETZSCH LFA 457 MicroFlash). Laser Flash Analysis (LFA) is currently the primary technique used for direct measurement of a material's thermal diffusivity. It was first developed and utilized by Parker et al. in 1961 at the U.S. Naval Radiological Defense Laboratory in San Francisco, CA [69]. In LFA, a sample of known dimensions is placed in a stabilized test chamber or furnace and is subjected to a laser pulse (precision burst of heat), focused by a mirror directly underneath the sample. The heat from the pulse diffuses through the material and passes to an infrared receiver directly above the sample. The IR detector then measures the variation in temperature over time, or transient response, at the top side of the sample. The diffusivity is calculated from the time required for the temperature at the top side of the sample to reach half its maximum value, known as a half-time measurement [70].

$$\alpha = 0.1388\frac{d^2}{t_{1/2}} \tag{3.4}$$

The half-time measurement is a function of the square of sample thickness, d [m], the required half time, $t_{1/2}$ [s], and an empirically derived constant. LFA measurements are known to have an uncertainty of at most 10 %, though several researchers have applied adjustments to measuring techniques, and some have reported a reduction in uncertainty to as little as 1 % [71]. Correctional models have also been developed to reduce uncertainty, such as the Cape-Lehman Model, which accounts for finite pulse length, transient heat transfer, and heat loss effects [70].

An internal schematic of the LFA 457 can be seen in Fig. 3.15. The laser voltage is adjustable, and can be tailored depending on sample geometry and expected diffusivity. For example, if a thicker sample with low expected thermal diffusivity is tested, the laser pulse should be at higher voltage for better measurement resolution. Typically, LFA is conducted in a highly controlled environment, where the chemical composition of the atmosphere and the temperature in the test chamber are well-defined. The presence of air molecules in the test chamber, for example, could interact with and change the thermal properties of the sample. The LFA is equipped to purge its test chamber of air by a combination of vacuuming and flushing with inert gas (typically compressed nitrogen or argon gas). The dissipation of heat after a laser pulse is another concern. Liquid nitrogen contained in the dewar above the IR receiver acts as the primary heat sink for residual heat. In addition, deionized water maintained at ambient is continually circulated through the laser and furnace during measurement to protect laser and sensory equipment.

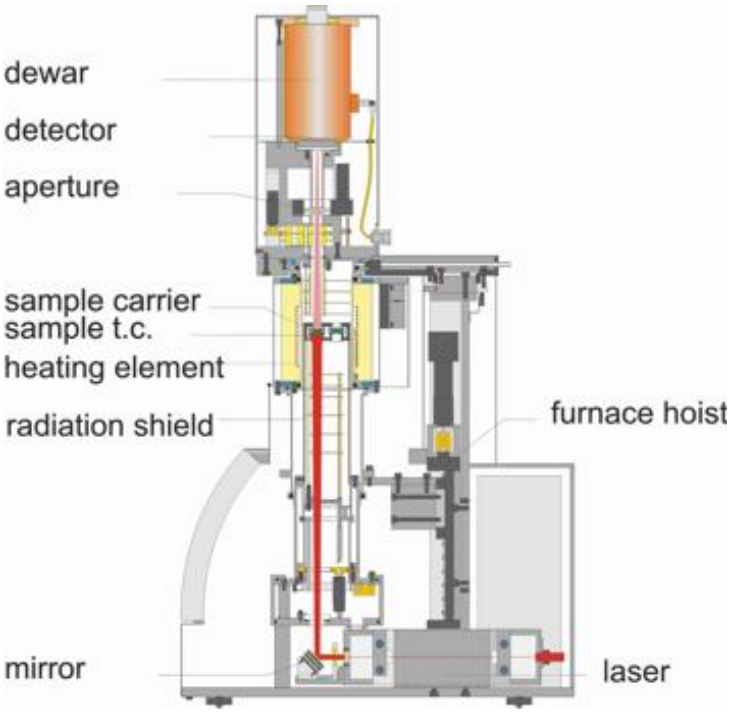

Fig. 3.15 an internal schematic of the NETZSCH LFA 457 MicroFlash. Courtesy www.netzsch-thermal-anlysis.com

The LFA has several different sample holder sizes in both square and circular shapes, and can be 10.0, 12.7, or 25.4 mm in diameter for circular holders and 8x8 mm^2 or 10x10 mm^2 for square holders. Most sample configurations allow for measurement of three samples at a time, with the exception of the 25.4 mm circular holder, which is measured alone. Additional holders can contain other samples, but at least one usually contains a reference sample (Pyroceram 9606) with known dimensions, density, and specific heat capacity. Reference samples are used during analysis to extract specific heat values for the tested sample, if desired. Explicitly, the specific heat of a sample can be inferred by measuring the thermal diffusivity in a reference sample of known specific heat and comparing it to the thermal diffusivity in a sample of unknown specific heat. Measureable sample thickness depends on expected thermal diffusivity and ranges from 0.05-5 mm, with higher expected diffusivity samples allowing for greater thickness. The measureable

thermal diffusivity ranges from 0.01-1000 mm^2/s, and the furnace temperature can range from -125°C to 1100°C, with heating/cooling rates of 0.01-50 K/min.

3.5.1 Sample Preparation

Samples were prepared by graphite coating (dgf123, Miracle Power Products Corp) to eliminate any reflectivity on the material's surface. Graphite coating turns the sample's surface into a black body, meaning that it both absorbs and emits all incident radiation, with zero reflectivity. As radiation is emitted from the graphite coated top surface of the sample to the IR receiver, it represents the radiation emitted from the sample that was not absorbed. The sample should ideally be completely smooth and have parallel top and bottom surfaces, normal to the laser direction. Surfaces that are not smooth or level will reflect light angularly, creating radiative losses to the receiver and increasing measurement error. Along the path of the laser, disk-shaped radiation shields made of low-reflectivity material (silicon carbide and graphite) also prevent radiative losses. On the top side, an aperture precisely collimates and focuses radiation as it enters the IR receiver. Shots were taken at a set furnace temperature of 21 °C, using the Cape-Lehman + pulse correction model, a laser voltage of 2978 V, amplifier gain of 127, and laser filter of 0.1270 ms.

3.5.2 Measurement Analysis

The LFA 457 analysis software package uses measured thermal diffusivity values to extrapolate specific heat and thermal conductivity. Figure 3.16 shows a standard example of data analysis from an LFA measurement. In this case, if the sample measured has a known density, a plot of thermal conductivity with respect to temperature can also be generated. A measurement's validity is evaluated by how well the approximated pulse correction model aligns with recorded laser voltage with respect to time (Fig. 3.16 bottom

right). Significant offset, especially at the onset of the laser pulse, invalidates the measurement.

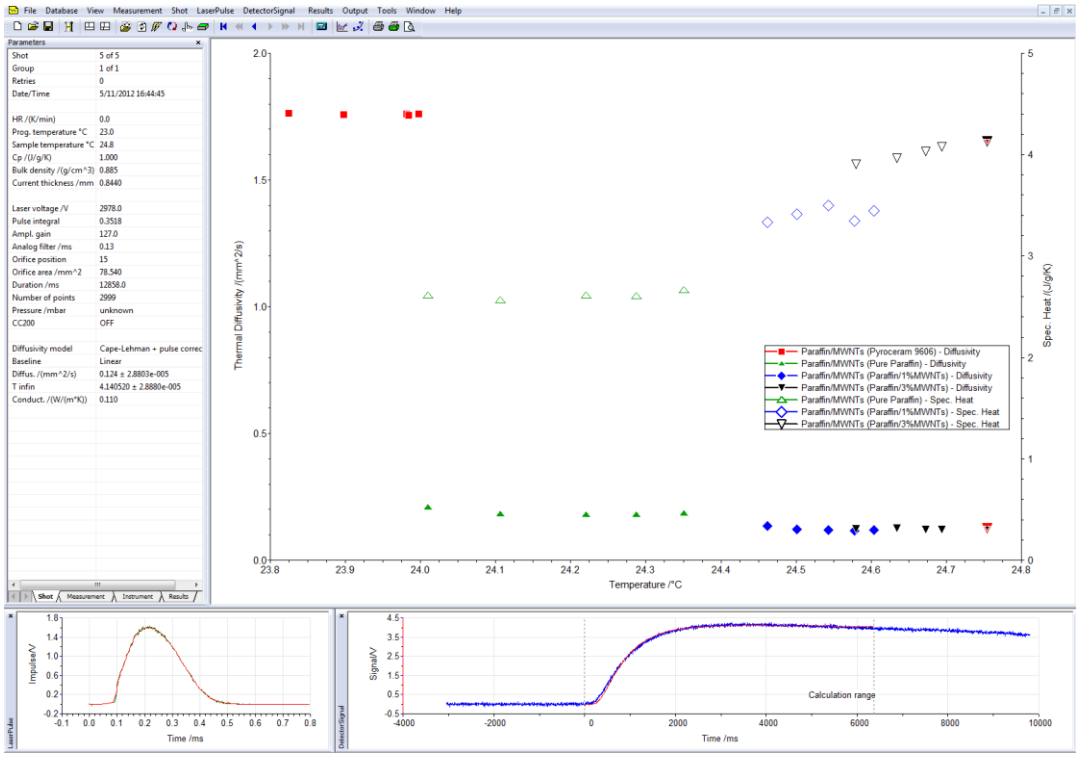

Fig. 3.16 Example data analysis of thermal diffusivity and specific heat vs. temperature for nanofluid samples and Pyroceram 9606 reference.

Chapter 4

Characterization Results and Discussion

Characterization testing was conducted to investigate the effects of particle addition on nanofluid thermal diffusivity and latent heat of fusion. In this chapter, results of the characterization study are presented, emphasizing the observed diameter-dependence of nanofluid latent heat of fusion. The three proposed mechanisms for latent heat reduction – interfacial liquid layering, Brownian motion, and particle clustering – are examined to assess their potential contribution to reduction below theoretical expectations. Finally, a method for predicting nanofluid latent heat of fusion is described, considering a dependence on particle size.

4.1 LFA Thermal Diffusivity Characterization Results

According to EMT, nanofluid thermal diffusivity should increase linearly with particle addition. Although no distinctive EMT has been developed, nanofluid thermal diffusivity is directly proportional to thermal conductivity, and should exhibit a similar degree of enhancement, as described by Eq. 2.20. Typically, nanofluid thermal diffusivity is measured indirectly through analysis of specific heat, thermal conductivity, and density. The original intention of this research, however, was to indirectly measure nanofluid thermal conductivity through direct measurement of thermal diffusivity, specific heat, and density. Particle size dependence on thermal diffusivity was not considered; hence, all nanofluid samples tested contained 15.5 nm diameter MWNTs.

Since nanofluid density and thermal conductivity are expected to follow traditional EMT, variations in nanofluid thermal conductivity beyond traditional theory can be

described by modified thermal conductivity EMT. The LFA characterization study results indicate a significant increase in thermal diffusivity for 0.2 % and 1 % volume fraction samples, beyond effective diffusivity corresponding to Maxwell 3ϕ limit conductivity enhancement. Shown normalized by base fluid diffusivity in Fig. 4.1, the resulting values show better agreement with effective thermal diffusivity calculated using Nan et al.'s thermal conductivity EMT for high aspect ratio particles [38, 42]. The Kapitza resistance used in Nan et al.'s model was 10^{-8} m^2K/W [60]. Particle shape was given by a defined particle major axis (length) of a_{33}=6.5e-6, and minor axis (outer diameter) of a_{11}=15.5e-9.

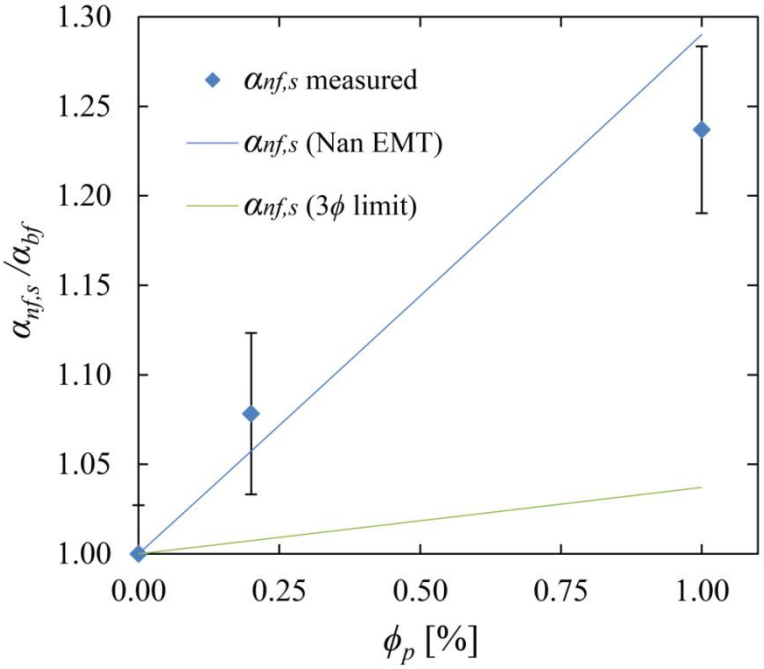

Fig. 4.1 Normalized nanofluid thermal diffusivity with respect to particle volume fraction. Theoretical nanofluid thermal diffusivity is estimated by Eq. 2.20, using nanofluid thermal conductivity given by the 3ϕ limit and Nan et al.'s model, divided by the product of density and specific heat EMT.

Reliable measurements for 0.5 % volume fraction samples were not obtained, for several reasons. Chiefly, sample preparation for LFA testing is a delicate process, requiring near flawless samples to acquire accurate measurements. The surfaces on both

faces of the sample must be parallel, planar, and within exact dimensions to fit in the sample holder. Any surface defects will affect the distribution of heat within the sample, which is assumed to diffuse uniformly through the material. Voids between the sample sides and sample holder base will allow laser leakage, which can invalidate a measurement. The method of sample preparation described in Chapter 3 was capable of consistently producing useful samples; however, LFA measurements require input parameters such as sample density and thickness, which were difficult to obtain without creating sample defects. For example, the paraffin-based samples were easily deformed by laboratory tweezers while conducting density measurements using the Archimedes kit. In addition, thickness measurements, acquired using a micrometer, created indentations in the sample surface. To ensure repeatability, at least five density and thickness measurements were acquired for each sample, increasing the possibility of creating defects. Once these measurements were obtained, the sample was also graphite coated. A set of three samples, including a Pyroceram 9606 reference, were coated simultaneously. Often, the stream of compressed graphite spray would move the sample, or even flip it over. Uncertainty introduced by uneven coating also led to invalid measurements.

LFA is also capable of specific heat measurements. Nevertheless, due to the difficulty of producing samples free of defects, accurate specific heat measurements could not be acquired. For thermal diffusivity measurements, the instrument uncertainty of the LFA is ± 3 %. This uncertainty increases to ± 7 % for specific heat measurements, demonstrating a much greater sensitivity to sample defects. For future studies, it is suggested that room temperature LFA measurements be conducted in the liquid sample holder for more accurate determination of paraffin nanofluid thermal diffusivity. However,

since the liquid holder does not support a Pyroceram reference sample, specific heat cannot be obtained with this method.

Using the liquid holder eliminates the need for excessive caution in sample preparation. Sample thickness is not required because the liquid holder thickness is always constant. Moreover, the sample itself does not have to be graphite coated. Sample defects are also not a concern, since the sample may be melted to conform to the holder. The only remaining precaution is the need for uniform contact between the holder base and the sample, and between the sample and holder lid. Any void in surface contact will have the same effect as a surface defect, causing heat to diffuse non-uniformly within the sample. The suggested sample volume to achieve ideal surface contact within the holder is approximately 60 μL. Room temperature samples can be prepared with the same method as outlined in Chapter 3 for liquid samples, and allowed to solidify in the holder.

4.2 Approximation of Nanofluid Thermal Conductivity

In order to estimate nanofluid thermal conductivity, the specific heat of the base fluid was needed. Since neither of the available instruments, the LFA and DSC, could be utilized to measure paraffin specific heat, samples were taken to NETZSCH Instruments North America in Burlington, Massachusetts. Using a low temperature DSC with controlled cooling, specific heat measurements were acquired. Outfitted with a liquid nitrogen dewar pressurizer (NETZSCH CC 300), the DSC furnace temperature was allowed to stabilize at subzero temperatures prior to entering the heating phase. Solid state measurements of paraffin specific heat were acquired in the range of -30 °C to 3 °C. Liquid state specific heat was also recorded in the range of 72 °C to 115 °C. The resulting measurements and associated instruments used are included in Table 4.1.

Using an averaged specific heat of pure paraffin from the values in Table 4.1, specific heat EMT can be applied (Eq. 2.19) to approximate nanofluid specific heat with respect to particle loading. An estimate of pure paraffin thermal conductivity is calculated with Eq. 2.20, using measured base paraffin density, thermal diffusivity, and specific heat. With an approximate base fluid thermal conductivity, nanofluid thermal conductivities are estimated at the volume fractions of samples tested in the LFA. Resulting thermal conductivity values, normalized by base fluid thermal conductivity, are shown in Fig. 4.2, along with theoretical limits given by the 3ϕ limit, HS upper bound, and Nan et al.'s EMT for 15.5 nm diameter suspended MWNTs.

Table 4.1 Specific heat measurements of pure sonicated paraffin taken at NEZTSCH Instruments North America. Liquid nitrogen (LN2) cooling was used to achieve stable DSC signal at subzero temperatures prior to heating. Solid and liquid state specific heat measurements were acquired.

Instrument	LN2 Dewar	Heating rate [K/min]	Cooling rate [K/min]	Temperature Range [°C]	Solid state c_p [J/gK]	Liquid state c_p [J/gK]
STA 449 F3	CC 300	10	10	-30 – 115	1.895	2.242
					1.881	2.303
DSC 200 F3					1.761	2.144
					1.759	2.145

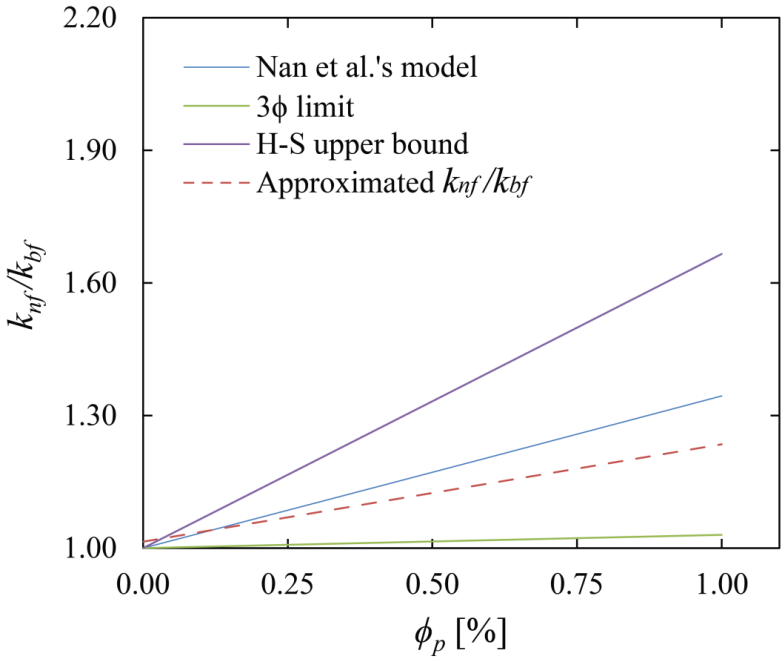

Fig. 4.2 Normalized nanofluid thermal conductivity with respect to particle volume fraction. The dashed line represents a linear trend line of thermal conductivity values at 0.2 and 1 % volume fraction, estimated from Eq. 2.20 using thermal diffusivity and density measurements, and specific heat EMT. Also included are theoretical bounds generated by the 3ϕ limit, H-S theory, and Nan et al.'s modified EMT.

The thermal conductivity of the MWNTs was defined as $k_p/k_{bf} \approx 100$ which is within experimental estimates for MWNTs measured using pulsed photothermal reflectance [74]. The high aspect ratio MWNTs lead to nanofluid thermal conductivity enhancement beyond the 3ϕ limit, and show better agreement with Nan's model.

With the acquisition of a liquid nitrogen dewar for DSC measurements, study of nanofluid specific heat could provide a more definitive approximation of thermal conductivity. Since nanofluid thermal diffusivity and density have been characterized with particle addition, future measurement of nanofluid specific heat is suggested to provide indirect estimations of thermal conductivity. On the other hand, thermal conductivity may be measured directly, using transient hot wire analysis [75] or with the KD2 Pro (Decagon

Devices, Inc.) [63], which is a handheld thermal property analyzer based on the transient hot wire method.

4.3 DSC Latent Heat of Fusion Characterization Results

DSC measurements show that at each volume fraction tested, sample latent heat of fusion reduces for nanofluids of smaller particle diameter. At 1 % particle volume fraction, nanofluids with 15.5 nm diameter MWNTs exhibit an additional 10 % reduction below the mass loss prediction (Eq. 2.23). Shown in Fig. 4.3, all samples exhibit linear latent heat reduction with particle loading, below that expected by traditional EMT.

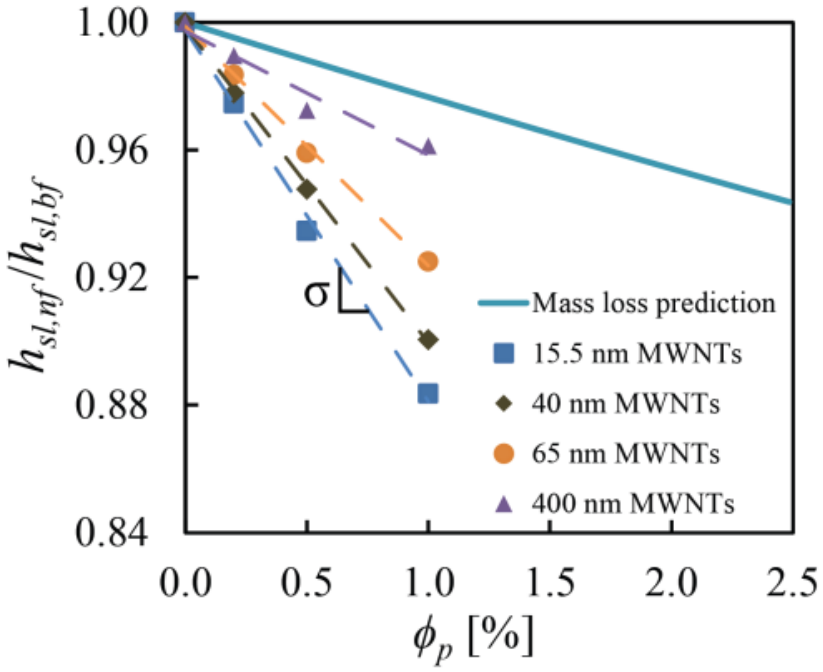

Fig. 4.3 Normalized nanofluid latent heat of fusion versus particle volume fraction measured by DSC, where σ is defined as the normalized latent heat reduction rate. At constant particle volume fractions, nanofluid latent heat is shown to reduce with decreasing particle size.

Looking at a single volume fraction, latent heat is observed to reduce with smaller diameter particles in suspension. Therefore, additional reduction below the mass loss prediction is shown to be independent of particle volume fraction. Defining σ as latent heat reduction

rate with respect to particle volume fraction, the magnitude of reduction rates is shown to increase as particle diameter decreases (Fig 4.4). Several experimental studies also appear to follow this trend [47, 49, 50]. However, the nanofluids investigated by both Wu et al. and Ho and Gao contain spherical particles, which may explain observed differences from the measured results. Moreover, Zeng et al. do not report the diameter of the nanowires used in their study. Instead, an average value was estimated from provided SEM images, which may not serve as an accurate representation. Nevertheless, the strong dependence on particle diameter suggested by these results serves as a basis for assessing the contributions of the proposed latent heat reduction mechanisms.

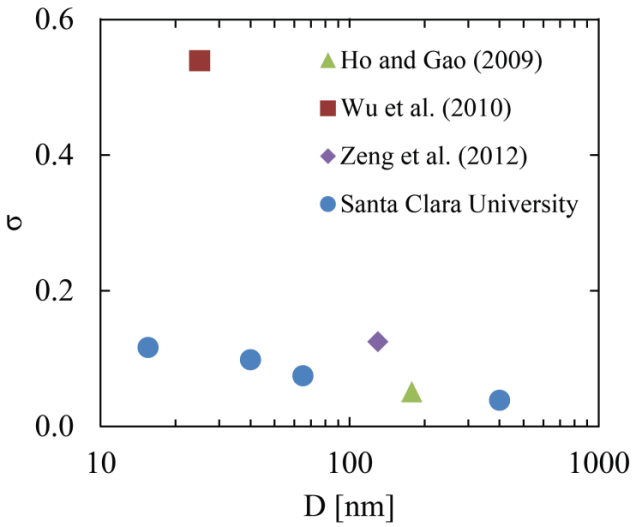

Fig. 4.4 Normalized latent heat of fusion reduction rate, σ, with respect to particle diameter (logarithmic scale) for measured nanofluid samples and reported literature values.

4.4 Latent Heat Reduction Mechanisms

As defined by the mass loss prediction, nanofluid latent heat of fusion is reduced from the base value due to the volume of particles in the medium not contributing to latent heat. In accordance with experimental findings, latent heat reduction beyond the mass loss prediction suggests that aside from nanoparticle volume, there is additional volume not

contributing to latent heat. It is proposed that this additional volume is represented by effective volumes of strained base fluid molecular structure, which require less energy to break down during melting. Molecular strain is induced by the following interface phenomena: interfacial liquid layering, Brownian motion, and particle clustering. Each of these effects is diameter-dependent, and has a greater impact with reduced particle size. Therefore, these phenomena are considered as mechanisms for the diameter-dependent nanofluid latent heat reduction observed. The contribution of each reduction mechanism is analyzed by approximating the respective strained region volume generated, and comparing to the strained volume required to explain observed reduction.

4.4.1 Interfacial Liquid Layering

The first mechanism investigated, interfacial layering, facilitates latent heat reduction through weakening of base fluid molecular structure. At the interface, van der Waals forces attract nearby base fluid molecules and form a densely packed, more ordered layer. During this process, molecular bonds between surrounding base fluid molecules are strained, and require less energy to break down during melting. The effects of strain propagate normal to the interface, as the inverse of distance from the particle surface. An illustration of this process is shown in Fig. 4.5.

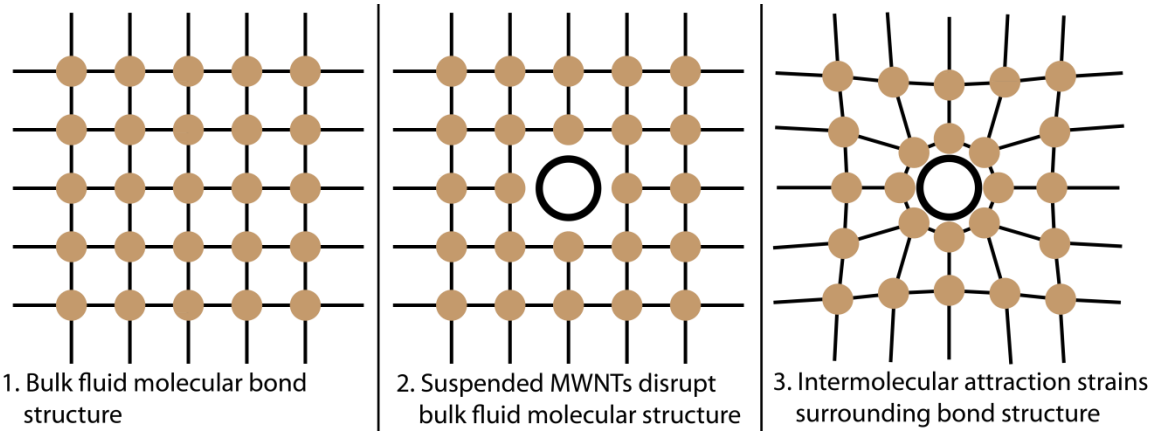

Fig. 4.5 Interfacial liquid layering of base fluid molecules around a particle in suspension. Van der Waals forces draw nearby molecules to the particle surface, generating strain in the surrounding base fluid molecular structure. The effects of strain propagate outward as the inverse of distance from the particle surface.

Since the number density of layered molecules increases with interface density, smaller diameter particles generate greater volumes of strained regions. To consider this effect theoretically, interface volume fraction (ϕ_i) is defined as the volume of interface phase (including both the densely packed layer at the interface and surrounding strained layer), over the total nanofluid volume,

$$\phi_i = \frac{V_i}{V_{nf}} \tag{4.1}$$

where ϕ is volume fraction, with i and p subscripts denoting interface and particle, respectively. Representing total nanofluid volume as a function of particle volume and particle volume fraction, Eq. 4.1 can be expressed as:

$$\phi_i = \phi_p \left(\frac{V_i}{V_p} \right) \tag{4.2}$$

Interface and particle volumes can be expressed through geometric functions of particle diameter (d_p), length (L), and interface phase width (w), as shown in Fig. 4.6.

$$\phi_i = \phi_p \left(\frac{\pi L \left[\left(\frac{d_p}{2} + w \right)^2 - \left(\frac{d_p}{2} \right)^2 \right]}{\pi L \left(\frac{d_p}{2} \right)^2} \right) = \phi_p \left(\frac{4w}{d_p} + \frac{4w^2}{{d_p}^2} \right) \tag{4.3}$$

After simplification, Eq. 4.3 demonstrates that interface volume fraction is inversely proportional to particle diameter when w/d_p is much less than unity.

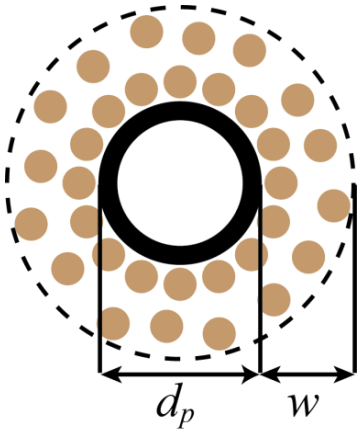

Fig. 4.6 Cross-section of MWNT with diameter d_p, surrounded by a densely packed layer and strained layer of base fluid molecules, with a collective interface phase width w.

It has been established from experimental studies and molecular dynamics simulations that the width of the densely packed layer (DPL) is no more than 1-2 nm [34, 35]. Since attractive forces dissipate normal to the particle surface, base molecules further away from the interface migrate shorter distances. The DPL width is thin (on the order of molecular spacings), demonstrating that the effect of van der Waals forces is relatively weak. Therefore, base molecules beyond the DPL do not experience significant movement, and the total interface phase width should scale on the same order as the DPL width. Consequently, interface volume fractions should also scale similarly to effective interface volume fractions consisting of only the DPL.

Interface volume fractions for each particle size tested can be evaluated from measured nanofluid latent heat, using a modified mass loss prediction for a ternary system. The nanofluid ternary system consists of base fluid, nanoparticles, and interface phase. As a minimum estimate of interface volume fraction, interface phase structure is assumed to be completely broken down and does not contribute to latent heat:

$$h_{sl,nf,tern} = \frac{\rho_{bf,s} h_{sl,bf} \left(1 - \phi_p - \phi_i\right)}{\rho_{nf}} \tag{4.4}$$

Using Eq. 4.4, interface volume fractions required to fit measured nanofluid latent heat are calculated and summarized in Table 4.2, for all particle diameters tested. DPL volume fractions are also calculated, using Eq. 4.3, assuming a DPL width of w = 2 nm. In Table 4.2, all interface volume fractions are shown normalized by particle volume fraction, and thus, are represented as ratios of either interface phase or DPL volume to individual particle volume. Also included are MWNT geometries and the required width of the interface phase to fit measured reduction, calculated from Eq. 4.3.

The resulting required interface volume fractions significantly overestimate interface volume fractions consisting of only the DPL. Corresponding required interface phase widths are on the order of particle diameter, which is highly inconsistent with approximations in literature [23]. Since strained regions within the interface phase are unlikely to occupy volumes two orders of magnitude greater than respective DPL volumes, interfacial layering effects cannot solely explain the degree of latent heat reduction observed.

Table 4.2 Interface volume fractions required to fit measured nanofluid latent heat for all particle sizes tested ($V_{i,req}/V_p$), calculated with Eqs. 4.2 and 4.4. Required interface volume fractions are compared to effective interface volume fractions consisting of a 2 nm thick densely packed layer ($V_{i,DPL}/V_p$). Interface volume fractions are normalized by particle volume fraction (ϕ_i/ϕ_p), and represented as ratios of interface volume to particle volume.

MWNT Diameter [nm]	MWNT Length [μm]	w Required to Fit $h_{sl,nf}$ [nm]	$V_{i,req}/V_p$	$V_{i,DPL}/V_p$
15.5	6.5	17.5	9.62	0.58
40.0	15.0	39.0	7.69	0.21
65.0	15.0	50.0	5.44	0.13
400.0	27.5	125.0	1.65	0.02

A correlation between interfacial liquid layering and measured latent heat can be made, considering the inverse proportionality to particle diameter in Eq. 4.3. As shown in Fig 4.7(a), each particle diameter independently shows a linear relation to latent heat reduction, but a weaker fit is demonstrated (r = -0.8625) when considering all particle diameters tested. Alternatively, a very strong correlation (r = -0.9729) among all particle diameters is seen in Fig. 4.7(b), considering a proportionality to the inverse square root of particle diameter. The proportionality to inverse square root of particle diameter was considered because it describes the diameter-dependency of particle diffusion due to Brownian motion. The strong correlation between this proportionality and observed latent heat reduction suggests that Brownian motion may have a significant role as a reduction mechanism.

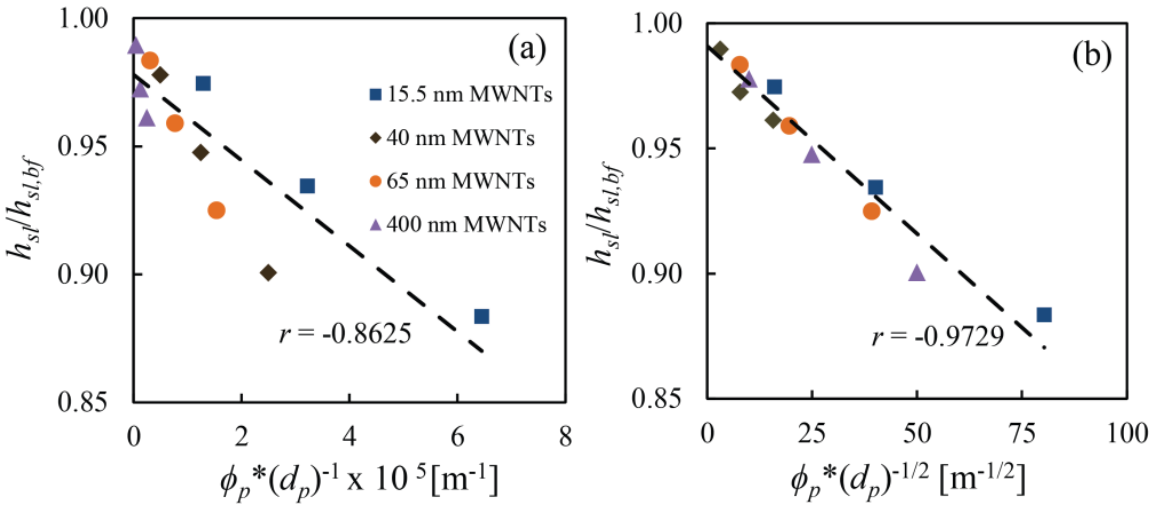

Fig. 4.7 Normalized nanofluid latent heat versus functions of particle diameter. (a) Plotted versus inverse particle diameter, representing interfacial liquid layering, with a correlation coefficient, r = -0.8625. (b) Plotted versus inverse square root particle diameter, a proportionality of Brownian diffusion, with r = -0.9729.

4.4.2 Brownian Motion

Similar to interfacial liquid layering, Brownian diffusion causes disruption of base fluid molecular structure as nanofluids undergo phase change, generating an effective sweep volume of weakened bond structure (Fig 4.8).

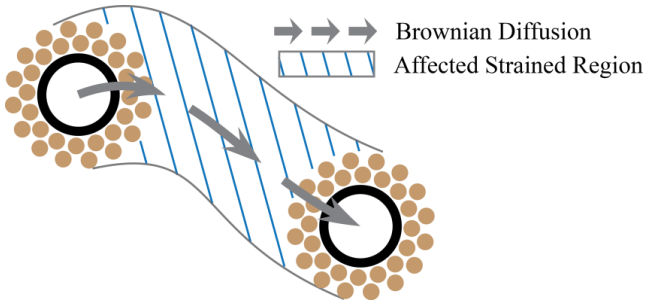

Fig. 4.8 Illustration of the sweep volume of strained base fluid molecular structure, generated by a MWNT undergoing Brownian diffusion.

Brownian motion refers to random movement of particles in a fluid which result in particle collisions that facilitate energy transfer through a direct solid-to-solid interaction. A theoretical analysis of the movement of Brownian particles was originally developed by Einstein [76]. Einstein's work became a validation of the molecular kinetic theory of heat, as it provided a method for determining the true size of atoms, which could be compared to Avogadro's number. Einstein defined the diffusion coefficient of a Brownian particle as a function of the Boltzmann constant, k_B, temperature and Stokes' law for the motion of a sphere in a viscous medium.

$$D = \frac{k_B T}{3\pi\mu d_p} \tag{4.5}$$

From Fick's first law, Einstein developed another expression for D, in terms of the mean square displacement in one dimension of a free Brownian particle during time t.

$$D = \left\langle \overline{x^2} \right\rangle / 2t \tag{4.6}$$

By combining these relations, the mean square displacement of a Brownian particle is given as a function of Avogadro's number.

Einstein's method was verified experimentally by Jean Baptiste Perrin [77], who recorded the position of a Brownian particle after successive equal time intervals, such as in Fig. 4.9. Perrin estimated the resulting mean square displacement, and using Einstein's theoretical approach, was able to approximate Avogadro's number to within ±8 % accuracy.

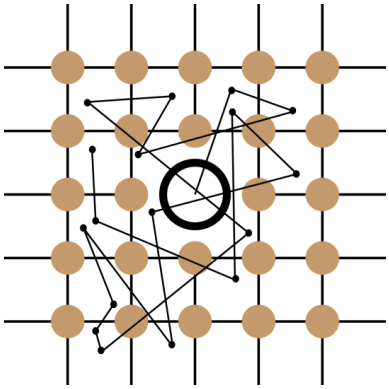

Fig. 4.9 Illustration of Jean Baptiste Perrin's experimental approach to observing Brownian motion. The position of a Brownian particle is recorded at successive equal time intervals, as shown by the nodes at each random change of direction.

By calculating average Brownian diffusion length, λ, the sweep volume generated by a single particle in suspension can be estimated. The magnitude of this Brownian sweep volume can be compared to the equivalent interface phase volume, $V_{i,req}$, required to fit measured nanofluid latent heat reduction – found using Eqs. 4.2 and 4.4. If both volumes are on the same order, Brownian movement can theoretically account for latent heat reduction not explained by liquid layering effects. The range of Brownian sweep volumes for cylindrical particles is at a minimum when diffusion is solely in the axial direction, and maximum when solely in the radial direction, as illustrated in Fig. 4.10. The range of

Brownian sweep volumes can be expressed as a function of average Brownian diffusion length, assuming a 2 nm thick interface phase width:

$$\pi L\left[\left(\frac{d_p}{2}+w\right)^2-\left(\frac{d_p}{2}\right)^2\right]+\pi\lambda\left(\frac{d_p}{2}+w\right)^2 \le V_{BrS} \le \pi L\left[\left(\frac{d_p}{2}+w\right)^2-\left(\frac{d_p}{2}\right)^2\right]+\lambda L\left(d_p+2w\right) \tag{4.7}$$

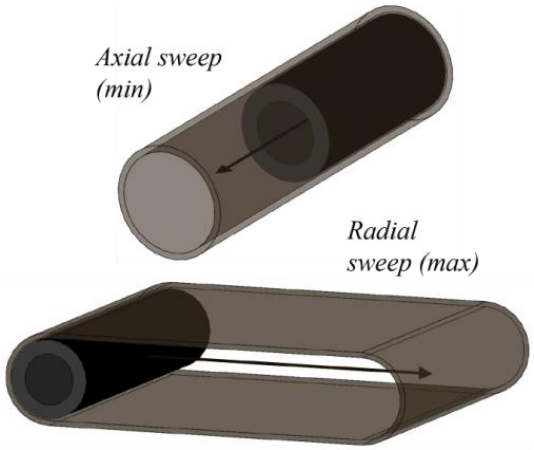

Fig. 4.10 Minimum and maximum Brownian sweep volumes for a single MWNT considering purely axial and radial diffusion, respectively.

Brownian motion can be either diffusive or ballistic, depending on the time scale of collisions between the particle and base fluid molecules. For Brownian motion in the diffusive regime, average Brownian diffusion length, λ [m], is inversely proportional to the square root of particle diameter,

$$\lambda = \sqrt{t} \times \sqrt{\frac{2k_B T}{3\pi\mu d_p}} \tag{4.8}$$

where μ is dynamic viscosity. The dynamic viscosity of paraffin was calculated from an empirical relation [10] as 4.34e-3 N·s/m^2, at an observed melting temperature of 40 °C. Eq. 4.8 is derived from the combination of Eqs. 4.5 and 4.6, as the square root of mean square displacement. If the particle is assumed to travel in a straight line in between observed collisions, the particle velocity can be expressed as:

$$v = \sqrt{\left\langle \overline{x^2} \right\rangle} / t_c \tag{4.9}$$

where t_c is the time between consecutive collisions. Einstein noted that as the time scale of particle collisions decreases without limit, particle speed must increase without limit for Brownian particles to move finite, observable distances. Therefore, Eq. 4.6 is only valid for Brownian particles undergoing collisions in the diffusive regime, at time scales longer than some arbitrarily short minimum time scale. This critical time scale was eventually defined as the momentum relaxation time, originally described by Paul Langevin [78], from the general solution for the time derivative of mean square displacement.

$$\frac{\overline{dx^2}}{dt} = \frac{RT}{N}\frac{1}{3\pi\mu d} + C\exp\left(-\frac{6\pi\mu d}{m}t\right) \tag{4.10}$$

Langevin notes that at the end of a time of order $m/6\pi\mu d$, the exponential term vanishes and Eq. 4.10 enters a constant regime, assuming the value of the first term. The time scale at the onset of the constant regime is the momentum relaxation time. For a particle of mass m, momentum relaxation time is given as:

$$\tau_p = \frac{m_p}{6\pi\mu d_p} \tag{4.11}$$

Particle mass can be calculated from the product of particle density and volume. The density of the MWNTs used in this study is 2.10 g/cm^3. For particle collision time scales much faster than the momentum relaxation time, the movement of a Brownian particle is dominated by its inertia, and the particle's motion is ballistic [79]. Eq. 4.11 describes the time for ballistic particles to decelerate and change direction, due to continuous collisions with base molecules that eventually overcome particle inertia.

To determine if nanofluid particle motion falls in the diffusive or ballistic regime, the time scale of particle/base molecule collisions was estimated. By approximating the collision frequency between particles, defined by Smoluchowski [80, 81],

$$q_{b-p} = \frac{2k_B T}{3\mu}\left[2 + \left(\frac{V_p}{V_b}\right)^{1/3} + \left(\frac{V_b}{V_p}\right)^{1/3}\right] \tag{4.12}$$

the collision rate, k_c, is given by

$$k_c = q_{b-p} N \tag{4.13}$$

where N is the number density, and subscripts b and p represent base fluid molecule and particle, respectively. The number density is defined as the number of particles within a given volume. For a given volume equivalent to the total nanofluid volume, base fluid volume fraction can be expressed as a function of base fluid number density:

$$\phi_{bf} = \frac{V_{bf}}{V_{nf}} = \frac{\pi d_b^{\,3}}{6} N \tag{4.14}$$

Thus, base fluid number density is given as:

$$N = \frac{6\phi_{bf}}{\pi d_b^{\,3}} \tag{4.15}$$

Finally, the collision time scale is defined as the inverse of the collision rate:

$$\tau_{b-p} = 1/k_c \tag{4.16}$$

Estimation of the collision frequency with Eq. 4.12 requires the volume of a base fluid molecule. The base fluid is assumed to have a chemical formula of $C_{21}H_{44}$, as this *n*-paraffin most closely resembles the melting temperature and density of paraffin observed in the characterization study [82]. The molar mass, M, of $C_{21}H_{44}$ is 296.576 g/mol or 0.297 kg/mol.

The diameter of a single base fluid particle may be calculated from the liquid state base fluid density:

$$\rho_l = \frac{M/A}{d_p^{\,3}} \tag{4.17}$$

where A is Avogadro's number, $6.022 \times 10^{23}\ \text{mol}^{-1}$. With a measured liquid paraffin density of 780.0 kg/m^3, the resulting base fluid molecule diameter is 8.58×10^{-10} m. Assuming the base particles are spherical, the volume of a single base fluid molecule is $3.31 \times 10^{-28}\ \text{m}^3$.

According to Eqs. 4.13 and 4.16, decreasing base fluid number density produces slower collision time scales. By Eq. 4.15, base fluid number density reduces with decreased base fluid volume fraction. Therefore, of the nanofluids tested, the longest collision time scales are calculated for 1 % particle volume fractions. Using the method described above, collision time scales for 1 % particle volume fraction nanofluids of varied particle diameter were calculated and compared to respective particle momentum relaxation time scales. As shown in Table 4.3, all MWNT particle geometries tested exhibit collision time scales at least three orders of magnitude faster than particle momentum relaxation time. Hence, all Brownian particles may be assumed to move ballistically in the base medium.

Table 4.3 Comparison of momentum relaxation time scales (Eq. 4.11) and particle/base molecule collision time scales (Eqs. 4.12-4.17), for Brownian particles of various diameter and length to determine ballistic/diffusive Brownian motion. Collision time scales are calculated assuming 1 % particle volume fraction.

MWNT Diameter [nm]	MWNT Length [μm]	τ_p [sec]	$\tau_{b\text{-}p}$ [sec]
15.5	6.5	4.06×10^{-9}	3.21×10^{-12}
40.0	15.0	2.42×10^{-8}	1.30×10^{-12}
65.0	15.0	3.93×10^{-8}	9.42×10^{-13}
400.0	27.5	4.44×10^{-7}	2.30×10^{-13}

In the ballistic regime, Eq. 4.8 is no longer a valid expression for average Brownian diffusion length. Instead, average ballistic Brownian diffusion length is given by [79]:

$$\lambda = t\sqrt{\frac{k_B T}{m_p}} \tag{4.18}$$

Compared to Eq. 4.8, which is proportional to the square root of time, ballistic Brownian diffusion length is directly proportional to time, which will lead to greater estimates of Brownian sweep volume. However, calculation of Brownian sweep volume requires a diffusion time of physical significance, since an arbitrary time scale cannot be applied.

The momentum relaxation time is an appropriate time scale because it signifies the maximum predictable range of Brownian movement. For example, in the case where a Brownian particle's movement is one-dimensional, there is equal probability for the particle to move in a forward (positive) or backward (negative) direction. Thus, the average distance the particle moves over time, relative to its initial position, is zero. Typically, mean square displacement is utilized to estimate absolute diffusion length; however, it cannot determine the maximum relative distance the particle travels from its initial

position. Swept volumes of base fluid are likely to overlap as Brownian particles change direction. If an arbitrary time scale is used, intersecting Brownian pathways will produce an overestimation of Brownian sweep volumes. Therefore, the furthest predictable distance a particle travels from its origin is given by the particle's initial diffusion length. Thus, the largest measureable nonintersecting sweep volume is defined over the momentum relaxation time.

Instead of approximating Brownian sweep volumes, required Brownian diffusion times to explain observed latent heat reduction can be estimated and compared to respective momentum relaxation times. Axial and radial Brownian sweep volumes are fit to required interface phase volumes, $V_{i,req}$, to calculate required average diffusion length (Eq. 4.7). Required diffusion lengths are applied to Eq. 4.18 to calculate ranges of required ballistic diffusion times. A comparison of the resulting time scales is shown in Fig. 4.11, demonstrating that required ballistic diffusion time scales are too slow for Brownian motion to explain the measured reduction in nanofluid latent heat of fusion.

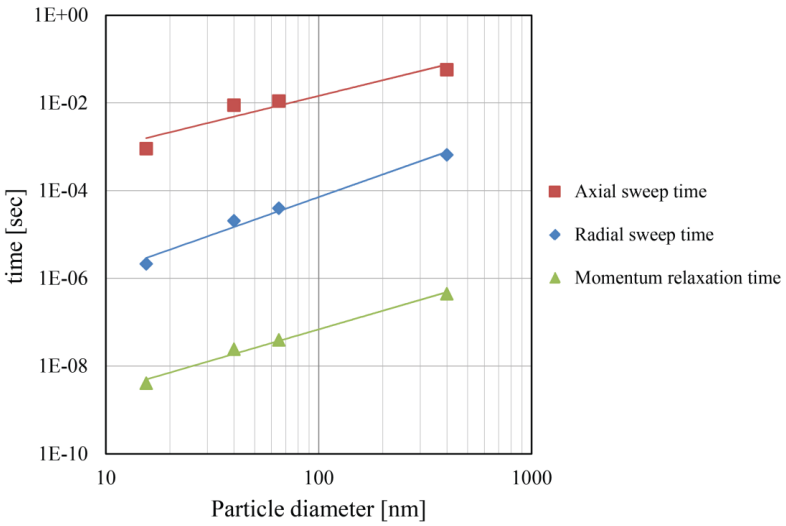

Fig. 4.11 Approximate time scales required for axial and radial Brownian sweep volumes of various diameter MWNTs to explain observed latent heat reduction, compared to respective momentum relaxation time scales.

Estimated momentum relaxation time scales are at least two orders of magnitude faster than required Brownian diffusion time scales. This discrepancy is even larger considering that Brownian sweep volumes intersect during diffusion, and would require much longer time scales to produce nonintersecting pathways. It is unlikely that additional sweep volume beyond the particle's predictable diffusion range could account for the orders of magnitude deficiency. Therefore, like interfacial liquid layering, Brownian motion cannot solely explain the degree of reduction observed.

4.4.2.1 Method of Approximating Nanofluid Latent Heat of Fusion

According to the strong correlation demonstrated in Fig. 4.7(b), observed latent heat reduction is well-described by a dependency on the inverse square root of particle diameter. This relationship was the basis for considering Brownian motion as a reduction mechanism. Consequently, the volume ratios $V_{i,req}/V_p$ in Table 4.2, defined as required interface volume fraction normalized by particle volume fraction, can also be described by a power function trend line of the form $V_{i,req}/V_p = C(d_p)^{-1/2}$ (Fig. 4.12). The proportionality constant C is calculated by least squares fitting, by setting $B = -1/2$ in the following set of equations:

$$
\begin{aligned}
&y = Cx^B, \\
&b = \frac{n\sum_{i=1}^{n}(\ln x_i \ln y_i) - \sum_{i=1}^{n}(\ln x_i)\sum_{i=1}^{n}(\ln y_i)}{n\sum_{i=1}^{n}(\ln x_i)^2 - (\sum_{i=1}^{n}(\ln x_i)^2)^2}, \\
&c = \frac{\sum_{i=1}^{n}(\ln y_i) - b\sum_{i=1}^{n}(\ln x_i)}{n}, \\
&B \equiv b, \\
&C \equiv \exp(c)
\end{aligned}
\tag{4.19}
$$

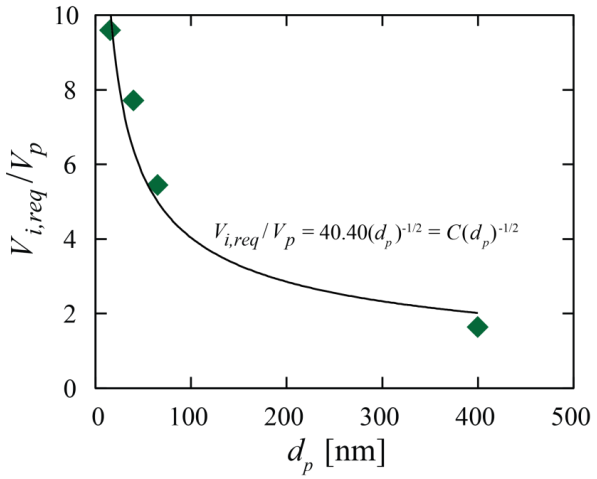

Fig. 4.12 Interface volume fractions required to explain observed latent heat reduction (Table 4.2), with respect to particle diameter. A power function trend line fit to the inverse square root of particle diameter shows good agreement with the calculated volume fractions.

Interestingly, if momentum relaxation time is defined as the time scale for Brownian diffusion, average diffusion length will be independent of particle diameter. For example, substituting Eq. 4.11 into Eq. 4.18 gives the average Brownian diffusion length during the momentum relaxation time:

$$\lambda = \frac{m_p}{6\pi\mu d_p}\sqrt{\frac{k_B T}{m_p}} \tag{4.20}$$

Expressing particle mass as the product of density and volume, Eq. 4.20 can be simplified,

$$\lambda = \frac{\rho\pi {d_p}^2 L}{24\pi\mu d_p}\sqrt{\frac{4k_B T}{\rho\pi {d_p}^2 L}} = \frac{1}{12\mu}\sqrt{\frac{\rho L k_B T}{\pi}} \tag{4.21}$$

eliminating all dependency on particle diameter. In order for Brownian diffusion length to exhibit proportionality to the square root of particle diameter, a constant diffusion time must be arbitrarily chosen. However, as previously described, diffusion time scales must have some physical significance for calculated diffusion lengths to be theoretically valid.

Although Brownian motion is incapable of explaining observed latent heat reduction, and Brownian diffusion length has been shown to be independent of particle diameter, the trend line in Fig. 4.12 appears to fit the estimated volume ratios well. Thus, strained phase volume over particle volume may be considered approximately proportional to the inverse square root of particle diameter. Methods of quantifying goodness of fit would require a greater sample size. Variable effects of nanofluid parameters such as particle geometry and base fluid dynamic viscosity are incorporated within the proportionality constant, *C*, which must be determined empirically. By expressing required interface volume fraction as a product of particle volume fraction, the inverse square root of particle diameter, and proportionality constant *C*, Eq. 4.4 may be used to approximate nanofluid latent heat of fusion. This approximation can be incorporated into a future modeling study of nanofluid phase change, which will be outlined in the following chapter. Additional research efforts are also needed to explain the strong correlation between latent heat reduction and the inverse square root of particle diameter.

4.4.3 Particle Clustering

Particle aggregation into high aspect ratio clusters has been described as the key mechanism for nanofluid thermal conductivity enhancement [23, 37, 83]. Percolation effects due to direct contact between aggregated particles explain thermal conductivity enhancement beyond traditional Maxwell theory. The effective volume of an aggregate cluster is larger than the volume of nanoparticles within the cluster, and exhibits higher thermal conductivity than the base fluid. Keblinski et al. state that even for densely packed aggregates, roughly 25 % of cluster volume is occupied by base fluid filling the voids between particles. Aggregates are formed as a result of inter-particle attraction due to van

der Waals forces. It is proposed that base fluid structure is strained as particles migrate towards each other. Strained base fluid volume within aggregate clusters can account for the interface volume required to explain observed latent heat reduction.

As described by Prasher et al. [37, 83], and illustrated in Fig. 4.13, aggregates are characterized by their radius of gyration (R_a).

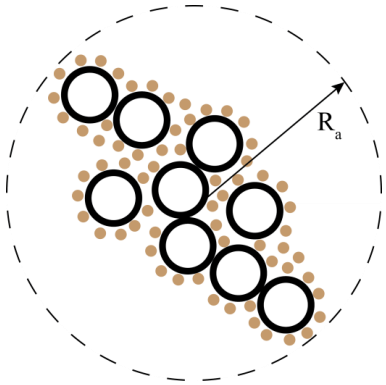

Fig. 4.13 High aspect ratio cluster of aggregated MWNTs in paraffin. Clusters are assumed to be spherical, and are characterized by their radius of gyration (R_a).

Radius of gyration is defined as the root mean square of the average radius from the cluster's center of mass. Prasher et al. define ϕ_{int} as the volume fraction of particles within aggregate clusters, and ϕ_a as the volume fraction of aggregates in the nanofluid. Hence, particle volume fraction can be defined as

$$\phi_p = \phi_{\text{int}}\phi_a \tag{4.22}$$

For a completely dispersed nanofluid, $\phi_{int} = 1$ and $\phi_p = \phi_a$, since each aggregate is composed of a single particle. On the other hand, $\phi_a = 1$ and $\phi_{int} = \phi_p$ for a completely aggregated nanofluid, since the entire nanofluid volume is composed of a single aggregate cluster.

Prasher et al. use Maxwell's EMT to estimate nanofluid thermal conductivity, replacing particle volume fraction and thermal conductivity with respective properties of the aggregate clusters.

$$\frac{k_{eff}}{k_{bf}} = \frac{(k_a + 2k_{bf}) + 2\phi_a(k_a - k_{bf})}{(k_a + 2k_{bf}) - \phi_a(k_a - k_{bf})} \tag{4.23}$$

An equation for aggregate thermal conductivity is also given, based on theoretical work by Wang et al. [84], accounting for effective conductivity enhancement due to percolation effects.

$$(1-\phi_{\text{int}})\frac{(k_{bf} - k_a)}{(k_{bf} + 2k_a)} + \phi_{\text{int}}\frac{(k_p - k_a)}{(k_{bf} + 2k_a)} = 0 \tag{4.24}$$

As described by Eq. 4.23, the thermal conductivity of a completely aggregated nanofluid approaches $k_{eff}/k_{bf} \approx 1+3k_a$, since $\phi_a = 1$. For a well-dispersed nanofluid, $\phi_a = \phi_p$, and Eq. 4.23 reduces to Maxwell's EMT (Eq. 2.1). Between these two extremes, thermal conductivity is predicted to peak at an optimum volume fraction of particles within aggregate clusters.

The volume fraction of particles within formed clusters, ϕ_{int}, is given by Potanin and Russel [85]:

$$\phi_{\text{int}} = (2R_a / d_p)^{d_f - 3} \tag{4.25}$$

where d_f is the fractal dimension of the aggregates, ranging from 1.75 to 2.5 [37]. Prasher et al. [37] assume d_f = 1.8, based on observations by Wang et al. [84] showing that nanofluids exhibit diffusion-limited cluster-cluster aggregation (DLCCA). Low range fractal dimensions represent a weak repulsive barrier, which is characteristic of DLCCA.

To investigate particle clustering's maximum potential contribution to latent heat reduction, ratios of maximum effective cluster volume to particle volume can be estimated, assuming a completely aggregated nanofluid. Since cluster volumes include the volume

of particles within the cluster, maximum cluster volume ratios should be compared to the following ratio:

$$\frac{V_{i+p,req}}{V_p} = \frac{V_{i,req} + V_p}{V_p} \tag{4.26}$$

Equation 4.26 is a more appropriate comparison than the required interface volume fractions in Table 4.2, which do not include particle volume. As mentioned previously, $\phi_a = 1$ for a fully aggregated nanofluid, and Eq. 4.22 gives $\phi_{int} = \phi_p$. Therefore, the maximum cluster radius of gyration is given by:

$$(R_a)_{\max} = (d_p/2)(\phi_p)^{1/(d_f-3)} \tag{4.27}$$

where ϕ_{int} in Eq. 4.25 has been replaced with particle volume fraction, ϕ_p. Assuming spherical clusters, calculated values of $(R_a)_{max}$ at various particle volume fractions allow for the estimation of maximum cluster volumes, $(V_a)_{max}$.

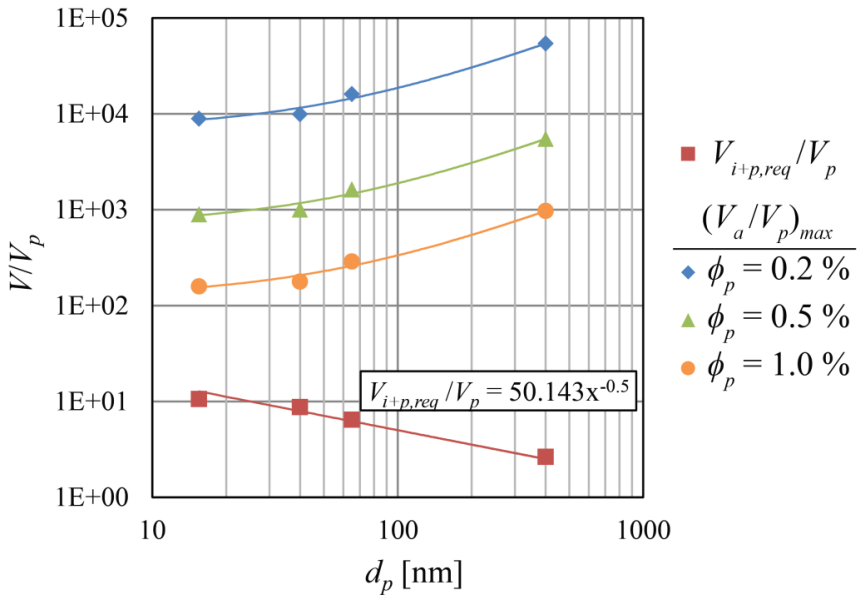

Fig. 4.14 Ratios of maximum aggregate volume to particle volume for various particle volume fractions, with respect to particle diameter. Maximum aggregate volume is calculated assuming a spherical cluster of radius $(R_a)_{max}$ (Eq. 4.27). Volume ratios are

compared to interface volume fractions required to explain latent heat reduction, normalized by particle volume fraction (Eq. 4.26).

As seen in Fig. 4.14, resulting maximum cluster volumes, normalized by particle volume, are orders of magnitude larger than required interface volume fractions (Eq. 4.26). Required interface volume ratios are normalized by particle volume; and thus, are represented by a single trend line similar to that in Fig. 4.12. On the other hand, maximum cluster volume ratios are shown for several particle volume fractions. Cluster volume ratios demonstrate linear fit with respect to diameter, as they describe a spherical to cylindrical volume ratio. Trend line approximations show that smaller particle volume fractions produce greater cluster volume fractions. Cluster volume fractions are also shown to increase with larger particle size, producing a greater divergence from required interface volume fraction. Despite these trends, larger particles at smaller volume fractions are less likely to aggregate.

Although the effect of strain within aggregate clusters is not considered in Fig. 4.14, the approximated scale of cluster volume fractions suggest that clustering is the principal mechanism for nanofluid latent heat reduction. Exact cluster volumes fractions required to fit required interface volume fractions can also be calculated, providing an estimate of the necessary degree of aggregation within the nanofluid. Firstly, the effective radius of volume $V_{i+p,\mathrm{req}}$ is calculated and substituted into Eq 4.25, in place of the cluster radius of gyration. Lastly, resulting values of ϕ_{int} are input into Eq. 4.22 to calculate required cluster volume fraction. These values are provided in Fig. 4.15, normalized by particle volume fraction, and are also well-described by the inverse square root of particle diameter. Figure

4.15 shows that cluster volume fraction must be at least an order of magnitude larger than particle volume fraction to account for the latent heat reduction observed.

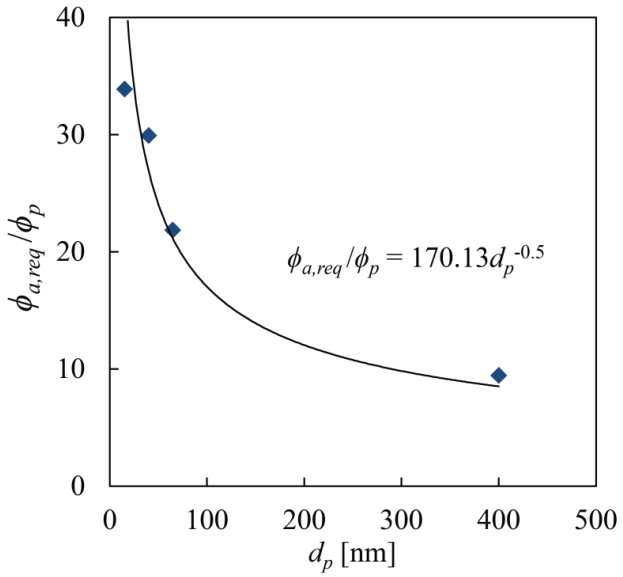

Fig. 4.15 Ratios of cluster volume fractions required to explain observed latent heat reduction to particle volume fraction, with respect to particle diameter. Approximated ratios scale proportionally with particle volume fraction.

Ultimately, additional research efforts are needed to further investigate particle clustering as a latent heat reduction mechanism. Direct measurement of nanofluid thermal conductivity, for example, will provide the effective values in Eqs. 4.23 and 4.24 needed to estimate cluster volume fraction. Approximations of cluster volume fraction can be compared to ratios provided in Fig. 4.15. In addition, molecular dynamics simulation should be conducted to provide a clearer understanding of the proposed reduction phenomena.

Chapter 5

Optimization Model for Nanofluid PCM

Upon characterization of nanofluid thermal properties, an application-based study of nanofluid PCMs was conducted. Since the developed nanofluids are intended for use in TES applications, it is important to consider effects of measured thermal properties on TES performance. In this chapter, observations from the study of nanofluid TES performance are presented. Additionally, the motivation for developing a predictive model of nanofluid phase change is explained. Finally, governing discretized equations for a finite element model utilizing the enthalpy method are derived. The model will be implemented in future study of nanofluid PCMs for thermal storage applications.

5.1 Need for Model of Nanofluid Phase Change

Nanofluid phase change materials (PCMs) in thermal energy storage (TES) applications will be required to transfer a given amount of heat over a certain period of time. This operational principle can be defined as TES performance. Characterization of nanofluid thermal properties has demonstrated significant reduction in latent heat of fusion with particle addition. This reduction has an unknown effect on TES performance. For example, particle addition is expected to enhance thermal conductivity and diffusivity. Improving these properties increases the rate of heat transfer to and from a given mass of PCM, defined as charge/discharge rate. Particle addition also leads to a reduction of nanofluid latent heat, which decreases the amount of available energy in the PCM per unit mass. Although specific storage capacity is decreased, reduced latent heat also improves charge/discharge rate, because less energy is required for phase change. For example,

when two identical storage containers filled with nanofluid PCM of the same thermal conductivity but differing latent heat are heated, a greater volume of PCM with lower latent heat will melt in a given period of time. However, since the lower latent heat PCM has reduced specific storage capacity, the overall impact on TES performance is not readily discernible. An optimum particle volume fraction will need to be determined to maximize total energy transferred over a given duration. Particle diameter is another variable parameter with an unknown impact on TES performance. The significant effect of particle diameter on latent heat must also be considered to assess impacts on nanofluid TES performance.

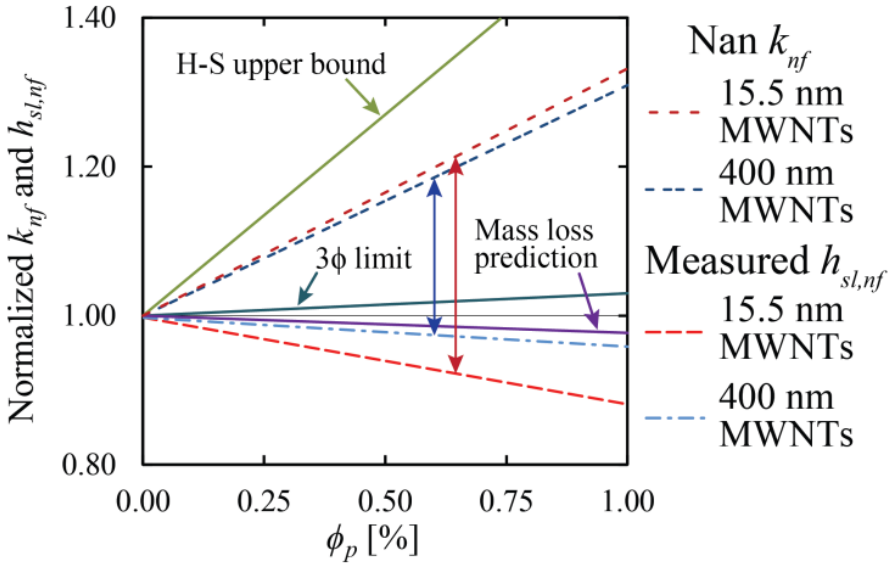

Fig. 5.1 Normalized nanofluid thermal conductivity (Nan et al.'s EMT) and measured latent heat of fusion with respect to particle volume fraction, for 15.5 nm and 400 nm diameter MWNTs.

To investigate effects of particle diameter and volume fraction on PCM storage performance, thermal conductivity enhancement and latent heat reduction of measured samples are examined. Latent heat reduction rates, σ from Fig. 4.4, give approximate linear reduction trends for 15.5 nm and 400 nm nanofluids. These particle geometries, with

respective lengths of 6.5 μm and 27.5 μm, are applied to Nan et al.'s model (Eqs. 2.11a-h) to estimate effective thermal conductivity enhancement. Resulting thermal properties are shown in Fig. 5.1, along with theoretical bounds for nanofluid conductivity and latent heat, including the H-S upper bound (Eq. 2.9), 3ϕ limit (Eq. 2.3), and the mass loss prediction (Eq. 2.23).

It is shown that nanoparticle size has a much greater impact on latent heat than thermal conductivity. Nan's model predicts a 7.2 % increase in the rate of thermal conductivity enhancement, while the rate of latent heat reduction increases by 300.3 %. The difference in thermal conductivity is mostly caused by the different aspect ratios of MWNTs used. The aspect ratio of the 15.5 nm diameter particles is roughly six times larger than that of the 400 nm diameter particles. Based on Nan et al.'s effective medium theory, there is no strong diameter dependency on thermal conductivity, unless nanoparticle diameters are small enough to support ballistic transport (1-2 nm) [29]. However, smaller diameter nanoparticles are more likely to aggregate into high aspect ratio clusters, and thus, indirectly enhance thermal conductivity [37].

On the other hand, particle diameter has been shown to have a significant impact on nanofluid latent heat. Overall, smaller particle diameter generates a greater divergence between effective normalized thermal conductivity and latent heat, which is illustrated by the two vertical arrows in Fig. 3. This difference suggests that nanofluids of smaller particle diameter can melt more PCM volume within a given period of time. However, the additional reduction of latent heat will reduce the amount of energy stored per unit mass. These counteracting effects complicate the quantitative assessment of nanofluid storage performance.

A numerical model is needed to determine the optimum particle diameter and volume fraction to maximize the amount of heat transferred over a given period of time. In accordance with our experimental findings, the numerical model should incorporate values for nanofluid latent heat of fusion that consider additional volume not contributing to phase change. The method for predicting nanofluid latent heat, presented in Chapter 4, can provide approximate values for the model.

5.2 Definition of Model Parameters and Discretization

The proposed model will simulate transient nanofluid phase change in an annular storage container. PCM in the outer annulus is heated convectively by working fluid in the inner annulus. Conduction heat transfer within the annulus is assumed to be axially symmetric, and thus, can be modeled as one-dimensional. Convection within the PCM is neglected. The model incorporates a numerical finite element approach, based on the enthalpy method [86]. The enthalpy method solves for stored internal energy at individual nodes, which is used to determine the phase of the material at each node, over iterative time steps. The configuration of nodes within the annulus is shown in Fig. 5.2.

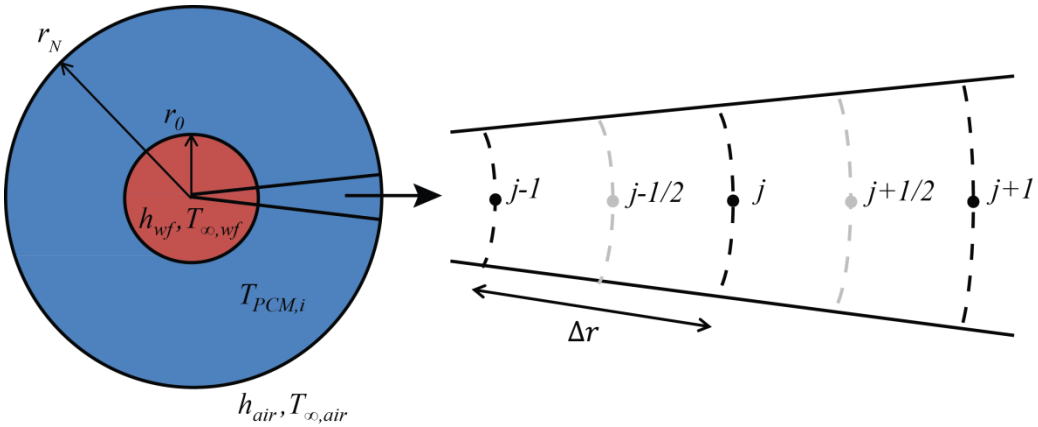

Fig. 5.2 Configuration of nodes within annular PCM storage container, at initial temperature $T_{PCM,i}$, heated convectively by a working fluid at constant temperature $T_{\infty,wf}$. Nodes range from r_o ($j=1$) at the heated interface to r_N (j=N) at the container wall, spaced apart by Δr steps.

Nodes are spaced at Δr steps, and range from r_o (j=1) at the heated interface to r_N (j=N) at the container wall. Matched conduction/convection boundary conditions are applied at the heated interface and container wall, assuming working fluid and ambient heat transfer coefficients of h_{wf} and h_{air}, respectively.

All discretized equations are derived from the first law of thermodynamics, neglecting work done due to PCM expansion during phase change.

$$\dot{Q} = \dot{U} \tag{5.1}$$

where U_{dot} is internal energy, given by:

$$\dot{U} = \rho c \frac{dT}{dt} \tag{5.2}$$

and Q_{dot} is the net heat transfer within the system:

$$\dot{Q} = \nabla^2 T = \frac{1}{r}\frac{\partial}{\partial r}\left(kr\frac{\partial T}{\partial r} \right) \tag{5.3}$$

Solid state enthalpy is defined as:

$$E = \int_{T_{init}}^{T_{melt}} \rho c_s \, d\tau \tag{5.4}$$

and liquid state enthalpy is given as:

$$E = \int_{T_{init}}^{T_{melt}} \rho c_s \, d\tau + \int_{T_{melt}}^{T_{final}} \rho c_l \, d\tau + \rho h_{sl} \tag{5.5}$$

where subscripts *init* and *final* denote initial and final states, and T_{melt} signifies melting temperature. In discretized form, solid and liquid state enthalpies are defined as:

$$E_j^i = \begin{cases} \rho c_s (T_j^i - T_i), & for \quad T_j^i < T_m \\ \rho c_s (T_j^i - T_i) + \rho c_l (T_j^i - T_m) + \rho h_{sl}, & for \quad T_j^i > T_m \end{cases} \tag{5.6}$$

A discretized equation for the enthalpy at inner nodes [j = 2 to j = (N-1)] is derived from the first law, considering the control volume (CV) in Fig. 5.3. Applying an energy balance, conduction into the CV is equal to the sum of internal energy and conduction out of the CV. The discretized form of this energy balance is given by:

$$q''_{cond}|_r\,(2\pi r_{j-1/2}L) - q''_{cond}|_{r+\Delta r}\,(2\pi r_{j+1/2}L) = \rho c_j^i[\pi L({r_{j+1/2}}^2 - {r_{j-1/2}}^2)]\left(\frac{T_j^{i+1} - T_j^i}{\Delta t}\right) \tag{5.7}$$

where subscripts r and j signify radial and nodal position, respectively, and superscript i is the iterative time step, initially at i = *1*. Since the surface area at each node increases moving outward from the center of the annulus, the radius at each node must be considered.

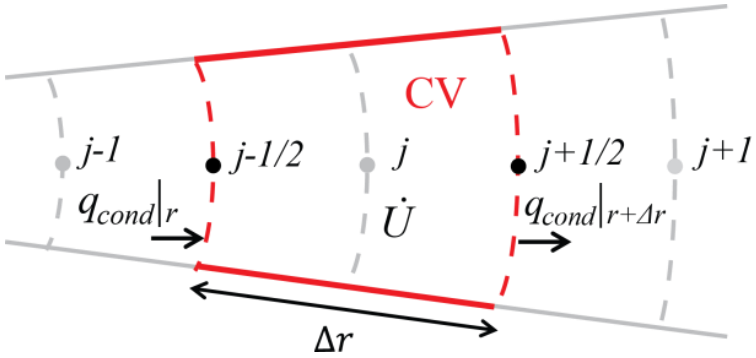

Fig. 5.3 Control volume defined to derive the discretized governing equation for the enthalpy at inner nodes [j = 2 to j = (N-1)].

The conduction terms in Eq. 5.7 may be represented by Fourier's law for one-dimensional conduction:

$$\frac{-k_{j-1/2}^i(2\pi r_{j-1/2}L)(T_{j-1} - T_j)}{\Delta r} + \frac{k_{j+1/2}^i(2\pi r_{j+1/2}L)(T_j - T_{j+1})}{\Delta r}$$
$$= \rho c_j^i[\pi L({r_{j+1/2}}^2 - {r_{j-1/2}}^2)]\left(\frac{T_j^{i+1} - T_j^i}{\Delta t}\right) \tag{5.8}$$

Distributing ρc within the time derivative, the term on the right hand side can be expanded,

$$\rho c[\pi L({r_{j+1/2}}^2 - {r_{j-1/2}}^2)]\left(\frac{T_j^{i+1} - T_j^i}{\Delta t}\right) = [\pi L({r_{j+1/2}}^2 - {r_{j-1/2}}^2)]\left(\frac{\rho c_j T_j^{i+1} - \rho c_j T_i + \rho c_j T_i - \rho c_j T_j^i}{\Delta t}\right) \tag{5.9}$$

in order to combine ρcT terms as discretized enthalpy terms, as defined in Eq. 5.6.

$$\frac{(\rho c_j T_j^{i+1} - \rho c_j T_i) + (\rho c_j T_i - \rho c_j T_j^i)}{\Delta t} = E_j^{i+1} - E_j^i \tag{5.10}$$

Squared radius terms at half nodes can also be expanded:

$$({r_{j+1/2}}^2 - {r_{j-1/2}}^2) = (r_j + \frac{\Delta r}{2})^2 - (r_j - \frac{\Delta r}{2})^2 = 2r_j \Delta r \tag{5.11}$$

and shown to reduce to the simple expression, $2r_j\Delta r$. Incorporating the simplified expressions of Eqs. 5.10 and 5.11 into Eq. 5.8, dividing out by πL and $2r_j\Delta r$, and rearranging terms, the final form of the governing discretized equation for the enthalpy at inner nodes is given as:

$$E_j^{i+1} = E_j^i + \left[\frac{\Delta t}{r_j(\Delta r)^2}(k_{j-1/2}^i r_{j-1/2})\right]T_{j-1}^i - \left[\frac{\Delta t}{r_j(\Delta r)^2}(k_{j+1/2}^i r_{j+1/2} + k_{j-1/2}^i r_{j-1/2})\right]T_j^i + \left[\frac{\Delta t}{r_j(\Delta r)^2}(k_{j+1/2}^i r_{j+1/2})\right]T_{j+1}^i \tag{5.12}$$

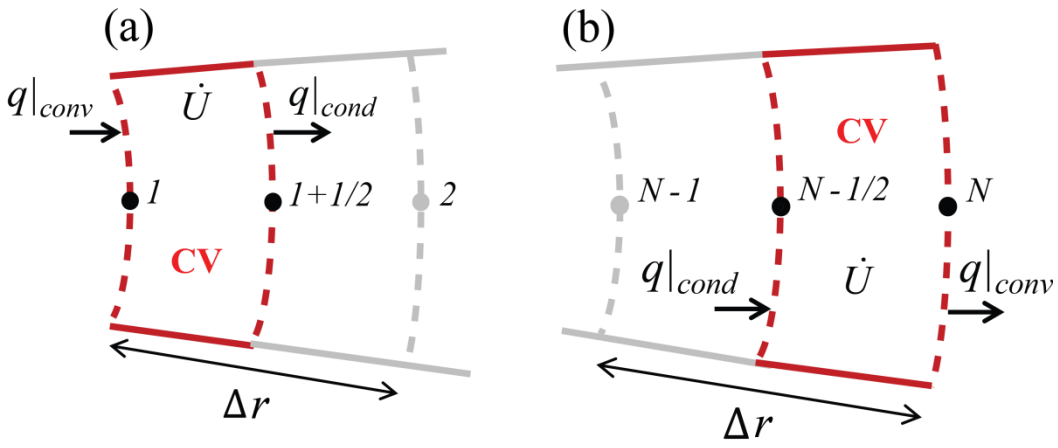

Fig. 5.4 Control volumes defined to derive discretized boundary conditions for the enthalpy at (a) the heated interface (j=1) (b) storage container wall (j=N).

Discretized enthalpy equations at the heated interface $j = 1$ and container wall $j = N$ are derived from boundary conditions matching conduction and convection. An energy balance is applied to each of the CVs in Fig. 5.4(a) and (b). Starting with Fig. 5.4(a), the appropriate energy balance is:

$$h_{wf}(2\pi r_1 L)(T_{\infty,wf} - T_1^i) - \frac{k_{1+1/2}^i (2\pi r_{1+1/2} L)(T_1^i - T_2^i)}{\Delta r} = \rho c_1 \left[\frac{\pi L (r_{1+1/2}{}^2 - r_1{}^2)(T_1^{n+1} - T_1^n)}{\Delta t} \right] \tag{5.13}$$

Using the same methods of simplification in Eqs. 5.9-5.11, Eq. 5.13 can be expressed in its final discretized form:

$$E_1^{i+1} = E_1^i - \left[\frac{2\Delta t}{r_{1+1/2}{}^2 - r_1{}^2} \left(h_{wf} r_1 + \frac{k_{1+1/2}^i r_{1+1/2}}{\Delta r} \right) \right] T_1^i + \left[\frac{2k_{1+1/2}^i r_{1+1/2} \Delta t}{\Delta r (r_{1+1/2}{}^2 - r_1{}^2)} \right] T_2^i + \left[\frac{2h_{wf} r_1 \Delta t}{r_{1+1/2}{}^2 - r_1{}^2} \right] T_{\infty,wf}^i \tag{5.14}$$

To derive the discretized boundary condition at the container wall, the energy balance for the control volume in Fig. 5.4(b) is given as:

$$\frac{k_{N-1/2}^i (2\pi r_{N-1/2} L)(T_{N-1}^i - T_N^i)}{\Delta r} - h_{air}(2\pi r_N L)(T_N^i - T_{\infty,air}) = \frac{\rho c_N \pi L (r_N{}^2 - r_{N-1/2}{}^2)(T_N^{i+1} - T_N^i)}{\Delta t} \tag{5.15}$$

and the final discretized equation takes the form:

$$E_1^{i+1} = E_1^i + \left[\frac{2k_{N-1/2}^i r_{N-1/2} \Delta t}{\Delta r (r_N{}^2 - r_{N-1/2}{}^2)} \right] T_{N-1}^i - \left[\frac{2\Delta t}{r_N{}^2 - r_{N-1/2}{}^2} \left(\frac{k_{N-1/2}^i r_{N-1/2}}{\Delta r} + h_{air} r_N \right) \right] T_N^i + \left[\frac{2h_{air} r_N \Delta t}{r_N{}^2 - r_{N-1/2}{}^2} \right] T_{\infty,air}^i \tag{5.16}$$

Lastly, the final discretized equations in Eqs. 5.12, 5.14, and 5.16, can be organized in a tridiagonal matrix (Eq. 5.17), which constitutes the base of the numerical model.

Solved enthalpy values at each node and iterative time step are used to solve for temperatures, liquid volume fraction λ, and thermal conductivity at the following time step. Table 5.1 provides a summary of the appropriate equations to estimate these properties, given different ranges of solved enthalpy values. Liquid volume fraction is zero when the material is in solid state, and 1 when in liquid state. When the temperature of the material has reached melting point, the material enters a "partial mush" state. In this mush state, the liquid volume fraction is defined as the fraction of stored enthalpy over the enthalpy required for the material to fully melt. Therefore, liquid volume fraction is an indicator of the material's state, and its progress towards melting during phase change. Equations for temperature were derived from Eq. 5.6. Thermal conductivity in the particle mush state is taken from Alexiades and Solomon [86], signifying a "sharp front" melting interface, with layers of solid and liquid in a serial arrangement.

Table 5.1 Equations to calculate temperature, liquid volume fraction λ, and thermal conductivity, based on ranges of nodal enthalpy values calculated from the tridiagonal matrix (5.17). The three ranges of enthalpies signify material in solid, partial mush, and liquid state.

Solver Condition	T_j^{i+1}	λ_j^{i+1}	k_j^{i+1}
$0 \le E_j^{i+1} < \rho c_s (T_{melt} - T_{init})$	$T_{init} + \frac{E_j^{i+1}}{\rho c_s}$	0	k_s
$\rho c_s (T_{melt} - T_{init}) \le E_j^{i+1} < \rho c_s (T_{melt} - T_{init}) + \rho h_{sl}$	T_{melt}	$\frac{E_j^{i+1} - \rho c_s (T_{melt} - T_{init})}{\rho h_{sl}}$	$\left(\frac{\lambda_j^{i+1}}{k_l T_{melt}} + \frac{1 - \lambda_j^{i+1}}{k_s T_{melt}} \right)^{-1}$
$\rho c_s (T_{melt} - T_{init}) + \rho h_{sl} \le E_j^{i+1}$	$\frac{E_j^{i+1} - \rho (h_{sl} - c_s T_{init} - c_l T_{melt})}{\rho (c_s + c_l)}$	1	k_l

(5.17)

$$
\begin{bmatrix} E_1^{i+1} \\ E_2^{i+1} \\ \vdots \\ E_{N-1}^{i+1} \\ E_N^{i+1} \end{bmatrix} = \begin{bmatrix} E_1^{i} \\ E_2^{i} \\ \vdots \\ E_{N-1}^{i} \\ E_N^{i} \end{bmatrix} +
$$

$$
\begin{bmatrix}
-\dfrac{2\Delta t}{r_{1+1/2}^{\,2} - r_1^{\,2}}\left(h_{wf} r_1 + \dfrac{k_{1+1/2}^{i} r_{1+1/2}}{\Delta r}\right) & \dfrac{2k_{1+1/2}^{i} r_{1+1/2}\Delta t}{\Delta r(r_{1+1/2}^{\,2} - r_1^{\,2})} & 0 & \cdots & 0 \\
0 & -\dfrac{\Delta t}{r_2(\Delta r)^2}(k_{2+1/2}^{i} r_{2+1/2} + k_{2-1/2}^{i} r_{2-1/2}) & \dfrac{\Delta t}{r_2(\Delta r)^2}(k_{2+1/2}^{i} r_{2+1/2}) & & \\
\vdots & \ddots & \ddots & \ddots & \vdots \\
0 & \cdots & 0 & \dfrac{\Delta t}{r_{N-1}(\Delta r)^2}(k_{N-1+1/2}^{i} r_{N-1+1/2} + k_{N-1-1/2}^{i} r_{N-1-1/2}) & 0 \\
0 & \cdots & 0 & 0 & \dfrac{2k_{N-1/2}^{i} r_{N-1/2}\Delta t}{\Delta r(r_N^{\,2} - r_{N-1/2}^{\,2})}
\end{bmatrix}
$$

$$
* \begin{bmatrix} T_{\infty,wf}^{i} \\ T_1^{i} \\ \vdots \\ T_N^{i} \\ T_{\infty,air}^{i} \end{bmatrix}
$$

Chapter 6

Conclusion and Future Work

6.1 Novel Contributions

The thermal properties of paraffin-based nanofluids containing multi-walled carbon nanotubes (MWNTs) have been investigated, utilizing differential scanning calorimetry (DSC) and laser flash analysis (LFA). Nanofluid thermal diffusivity was observed to increase with particle addition, demonstrating enhancement beyond traditional Maxwell effective medium theory (EMT). Although thermal diffusivity measurements showed agreement with Nan et al.'s EMT for high aspect ratio particles, the sample preparation and measurement technique applied introduced considerable uncertainty. Suggested methods for producing more accurate LFA measurements have been provided.

The latent heat of fusion of nanofluid samples containing various diameter multi-walled nanotubes was observed to reduce below theoretical expectations. Latent heat reduction below the mass loss prediction suggests that beyond particle volume, there is additional nanofluid volume not contributing to phase change. The rate of nanofluid latent heat reduction, with respect to particle volume fraction, was shown to increase in magnitude with smaller diameter nanoparticles in suspension. The diameter-dependent reduction observed was attributed to interface phenomena, which strain and weaken base fluid molecular structure, decreasing the energy required for it to break down during melting. The nanofluid was modeled as a ternary system of base fluid, nanoparticles, and interface phase, and volume fractions of interface phase required to explain observed reduction were calculated.

Interfacial liquid layering was initially suggested as a mechanism for latent heat reduction, generating strain as base molecules are drawn to the particle surface by van der Waals forces. Liquid layering is dependent on interface density, and produces interface phase volume fractions proportional to the inverse of particle diameter. Estimates of required interface phase volume fractions showed that the interfacial layer width must be on the order of particle diameter – a significant overestimation compared to literature approximations. Correlating observed latent heat reduction to inverse particle diameter showed a statistically significant, but weak fit. On the other hand, the inverse square root of particle diameter showed a very strong correlation to observed reduction, suggesting that Brownian motion may play a significant role in nanofluid phase change.

Strained regions of base molecular structure within Brownian sweep volumes were proposed to explain latent heat reduction. Estimation of Brownian sweep volume, however, requires a time scale to calculate average Brownian diffusion length. The distance a Brownian particle travels from its origin cannot be accurately defined beyond the length its initial change of direction. Therefore, the maximum diffusion time scale of valid physical meaning is given by the particle momentum relaxation time. Estimated momentum relaxation times were compared to times scales required for Brownian sweep volumes to fit previously calculated interface phase volumes. The resulting comparison showed that Brownian motion is too slow to account for observed latent heat reduction. Although Brownian motion was ruled out as a potential reduction mechanism, measured latent heat is well-described by a power function trend line of the form $V_{i,req}/V_p = C(d_p)^{-1/2}$. This power function can be used as an approximation for predicting the latent heat of nanofluids.

Lastly, particle clustering was considered as a latent heat reduction mechanism. It was suggested that base fluid structure is weakened as particles migrate towards each other in suspension. Aggregate cluster volumes are larger than the volume of particles within the cluster, and exhibit significantly higher effective thermal conductivity than the base fluid. Thus, clustering has been demonstrated as the key mechanism for nanofluid thermal conductivity enhancement. To determine the effect of clustering on nanofluid latent heat, maximum cluster volume fractions were calculated, assuming a completely aggregated system. Resulting cluster volume fractions were shown to be several orders of magnitude larger than those required to explain observed reduction. Although these scale approximations suggest that clustering is the primary mechanism for latent heat reduction, estimation of actual cluster volume fraction requires measurement of nanofluid thermal conductivity. Additional studies are needed to directly measure thermal conductivity and investigate effects of clustering on nanofluid latent heat.

The effect of nanofluid thermal properties on thermal energy storage performance was also presented. Particle diameter was shown to have a negligible effect on nanofluid thermal conductivity, opposed to the significant diameter-dependence of latent heat of fusion. Collectively, nanofluids with smaller diameter particles exhibit faster charge/discharge rates and reduced specific storage capacity. Defining storage performance as the amount of heat stored or extracted over a given duration, smaller particles were shown to theoretically improve storage performance. There is a limit, however, to the practicality of reduced specific storage capacity. Although more heat will be transferred at a faster rate, larger volumes of phase change material (PCM) will be needed to account for the reduced amount of energy stored per unit mass. It was

determined that a predictive modeling tool is necessary to define the optimum particle volume fraction and diameter to maximize nanofluid storage performance.

The framework of a one-dimensional finite element model of nanofluid phase change in an annular storage container was presented. Based on the enthalpy method, discretized equations and boundary conditions were derived from the first law of thermodynamics to calculate internal energy at iterative time steps. The development of a governing tridiagonal matrix is shown, including equations to calculate temperature and material phase at each node within the finite element mesh.

6.2 Future Work

In an effort to characterize nanofluid thermal properties, thermal diffusivity should be re-measured, incorporating refined techniques outlined in Section 4.1. Solid state thermal diffusivity measurements may be taken in the liquid sample holder to avoid uncertainty due to sample defects. In addition, equipping the DSC with a liquid nitrogen dewar will allow for direct measurement of solid state specific heat. Measurement of these thermal properties may also be applied to a future modeling study, and will provide a more comprehensive understanding of nanofluids thermal energy storage performance.

Additional study of latent heat reduction mechanisms will require direct measurement of nanofluid thermal conductivity. As outlined in Section 4.4.3, nanofluid thermal conductivity allows for estimation of cluster thermal conductivity and volume fraction. Cluster volumes fractions necessary for particle clustering to explain observed latent heat have been provided. Molecular dynamics simulation should also be conducted to confirm the proposed phenomenon of latent heat reduction due to strained base fluid structure. A definitive physical understanding of the mechanisms for nanofluid latent heat

reduction is needed, which should motivate a wide variety of research on this relatively unexplored topic.

Lastly, the finite element model presented in Chapter 5 may be applied to calculate optimum particle volume fraction and diameter to maximize nanofluid PCM energy storage performance. The model can also provide full melt and crystallization times in order to properly size a storage container for an intended application. Approximated values of nanofluid latent heat can be applied to the model, using the power function equation defined in Section 4.4.2.1. Ultimately, the model will serve as a predictive tool to provide a more accurate representation of nanofluid phase change than currently explained by theory.

References

[1] Dinçer, İ. and M.A. Rosen, *Thermal Energy Storage Systems and Applications, Second Edition*2011: John Wiley & Sons, Ltd.

[2] Cabeza, L.F., et al. *Review of Solar Thermal Storage Techniques and Associated Heat Transfer Technologies*. in *IEEE*. 2012.

[3] Kaygusuz, K. and T. Ayhan, *Experimental and theoretical investigation of combined solar heat pump system for residential heating.* Energy Conversion and Management, (1999) **40**: p. 1377-1396.

[4] Khudhair, A.M. and M.M. Farid, *A review on energy conservation in building applications with thermal storage by latent heat using phase change materials.* Energy Conversion and Management, (2004) **45**(2): p. 263-275.

[5] Yagi, J. and T. Akiyama, *Storage of thermal energy for effective use of waste heat from industries.* Journal of Materials Processing Technology, (1995) **48**: p. 793-804.

[6] Zhou, D., C.Y. Zhao, and Y. Tian, *Review on thermal energy storage with phase change materials (PCMs) in building applications.* Applied Energy, (2012) **92**: p. 593-605.

[7] Abhat, A., *Low temperature latent heat thermal energy storage: Heat storage materials.* Solar Energy, (1983) **30**(4): p. 313-332.

[8] Fang, Y., et al., *Preparation and characterization of novel nanoencapsulated phase change materials.* Energy Conversion and Management, (2008) **49**(12): p. 3704-3707.

[9] Zhang, H., X. Wang, and D. Wu, *Silica encapsulation of n-octadecane via sol-gel process: a novel microencapsulated phase-change material with enhanced thermal conductivity and performance.* J Colloid Interface Sci, (2010) **343**(1): p. 246-55.

[10] Kurnia, J.C., et al., *Improved design for heat transfer performance of a novel phase change material (PCM) thermal energy storage (TES).* Applied Thermal Engineering, (2013) **50**(1): p. 896-907.

[11] Fukai, J., et al., *Improvement of thermal characteristics of latent heat thermal energy storage units using carbon-fiber brushes: experiments and modeling.* International Journal of Heat and Mass Transfer, (2003) **46**(23): p. 4513-4525.

[12] Huang, M.J., et al., *Natural convection in an internally finned phase change material heat sink for the thermal management of photovoltaics.* Solar Energy Materials and Solar Cells, (2011) **95**(7): p. 1598-1603.

[13] Eastman, J.A., et al., *Anomalously increased effective thermal conductivities of ethylene glycol-based nanofluids containing copper nanoparticles.* Applied Physics Letters, (2001) **78**(6): p. 718.

[14] Hong, T.-K., H.-S. Yang, and C.J. Choi, *Study of the enhanced thermal conductivity of Fe nanofluids.* Journal of Applied Physics, (2005) **97**(6): p. 064311.

[15] Liu, M., M.C. Lin, and C. Wang, *Enhancements of thermal conductivities with Cu, CuO, and carbon nanotube nanofluids and application of MWNT/water nanofluid on a water chiller system.* Nanoscale Res Lett, (2011) **6**(1): p. 297.

[16] Mulligan, J.C., D.P. Colvin, and Y.G. Bryant, *Microencapsulated phase-change material suspensions for heat transfer in spacecraft thermal systems.* Journal of Spacecraft and Rockets, (1996) **33**(2): p. 278-284.

[17] Velraj, R., et al., *Heat Transfer Enhancement in a Latent Heat Storage System.* Solar Energy, (1999) **65**(3): p. 171-180.

[18] Agyenim, F., P. Eames, and M. Smyth, *Heat transfer enhancement in medium temperature thermal energy storage system using a multitube heat transfer array.* Renewable Energy, (2010) **35**(1): p. 198-207.

[19] Kleinstreuer, C. and Y. Feng, *Experimental and theoretical studies of nanofluid thermal conductivity enhancement: a review.* Nanoscale Res Lett, (2011) **6**(1): p. 229.

[20] Wang, X., X. Xu, and S.U.S. Choi, *Thermal Conductivity of Nanoparticle-Fluid Mixture.* Journal of Thermophysics and Heat Transfer, (1999) **13**(4): p. 474-480.

[21] Prasher, R., et al., *Measurements of nanofluid viscosity and its implications for thermal applications.* Applied Physics Letters, (2006) **89**(13): p. 133108.

[22] Buongiorno, J., et al., *A Benchmark Study on the Thermal Conductivity of Nanofluids.* Journal of Applied Physics, (2009) **106**(9): p. 14.

[23] Keblinski, P., R. Prasher, and J. Eapen, *Thermal conductance of nanofluids: is the controversy over?* Journal of Nanoparticle Research, (2008) **10**(7): p. 1089-1097.

[24] Maxwell, J., *A Treatise on Electricity and Magnetism*. Vol. 2. 1873, Oxford, UK: Clarendon Press.

[25] Jang, S.P. and S.U.S. Choi, *Role of Brownian motion in the enhanced thermal conductivity of nanofluids.* Applied Physics Letters, (2004) **84**(21): p. 4316.

[26] Koo, J. and C. Kleinstreuer, *A new thermal conductivity model for nanofluids.* Journal of Nanoparticle Research, (2005) **6**(6): p. 577-588.

[27] Prasher, R., P. Bhattacharya, and P. Phelan, *Thermal Conductivity of Nanoscale Colloidal Solutions (Nanofluids).* Physical Review Letters, (2005) **94**(2).

[28] Nelson, E., *Dynamical Theories of Brownian Motion*. Second ed2001: Princeton University Press.

[29] Keblinski, P., et al., *Mechanisms of heat flow in suspensions of nano-sized particles (nanofluids).* Internation Journal of Heat and Mass Transfer, (2002) **45**: p. 855-863.

[30] Shima, P.D., J. Philip, and B. Raj, *Role of microconvection induced by Brownian motion of nanoparticles in the enhanced thermal conductivity of stable nanofluids.* Applied Physics Letters, (2009) **94**(22): p. 223101.

[31] Eapen, J., et al., *Mean-Field Versus Microconvection Effects in Nanofluid Thermal Conduction.* Physical Review Letters, (2007) **99**(9).

[32] Babaei, H., P. Keblinski, and J.M. Khodadadi, *A proof for insignificant effect of Brownian motion-induced micro-convection on thermal conductivity of nanofluids by utilizing molecular dynamics simulations.* Journal of Applied Physics, (2013) **113**(8): p. 084302.

[33] Yu, W. and S.U.S. Choi, *The role of interfacial layers in the enhanced thermal conductivity of nanofluids: A renovated Maxwell model.* Journal of Nanoparticle Research, (2003) **5**: p. 167-171.

[34] Yu, C.J., et al., *Structure of interfacial liquids: X-ray scattering studies.* Physical Review E, (2001) **63**(2).

[35] Xue, L., et al., *Effect of liquid layering at the liquid–solid interface on thermal transport.* International Journal of Heat and Mass Transfer, (2004) **47**(19-20): p. 4277-4284.

[36] Joshi, A.A. and A. Majumdar, *Transient ballistic and diffusive phonon heat transport in thin films.* Journal of Applied Physics, (1993) **74**(1): p. 31.

[37] Prasher, R., P.E. Phelan, and P. Bhattacharya, *Effect of Aggregation Kinetics on the Thermal Conductivity of Nanoscale Colloidal Solutions (Nanofluid).* Nano Letters, (2006) **6**(7): p. 1529-1534.

[38] Nan, C.-W., et al., *Interface effect on thermal conductivity of carbon nanotube composites.* Applied Physics Letters, (2004) **85**(16): p. 3549.

[39] Hashin, Z. and S. Shtrikman, *Conductivity of Polycrystals.* Physical Review, (1963) **130**(1): p. 129-133.

[40] Hashin, Z. and S. Shtrikman, *A Variational Approach to the Theory of the Effective Magnetic Permeability of Multiphase Materials.* Journal of Applied Physics, (1962) **33**(10): p. 3125.

[41] Hamilton, R.L. and O.K. Crosser, *Thermal Conductivity of Heterogeneous Two-component Systems.* Industrial & Engineering Chemistry Fundamentals, (1962) **1**(3): p. 187-191.

[42] Nan, C.-W., et al., *Effective thermal conductivity of particulate composites with interfacial thermal resistance.* Journal of Applied Physics, (1997) **81**(10): p. 6692.

[43] Zhou, S.-Q. and R. Ni, *Measurement of the specific heat capacity of water-based Al_2O_3 nanofluid.* Applied Physics Letters, (2008) **92**(9): p. 093123.

[44] Shin, D. and D. Banerjee, *Enhancement of specific heat capacity of high-temperature silica-nanofluids synthesized in alkali chloride salt eutectics for solar thermal-energy storage applications.* International Journal of Heat and Mass Transfer, (2011) **54**(5-6): p. 1064-1070.

[45] Shin, D. and D. Banerjee, *Enhanced Specific Heat of Silica Nanofluid.* Journal of Heat Transfer, (2011) **133**(2): p. 024501.

[46] Wang, L., et al., *Enhancement of molar heat capacity of nanostructured Al_2O_3.* Journal of Nanoparticle Research, (2001) **3**: p. 483-487.

[47] Wu, S., et al., *Preparation and Melting/Freezing Characteristics of Cu/Paraffin Nanofluid as Phase-Change Material (PCM).* Energy Fuels, (2010) **24**: p. 1894-1898.

[48] Wang, X.-j., D.-s. Zhu, and S. yang, *Investigation of pH and SDBS on enhancement of thermal conductivity in nanofluids.* Chemical Physics Letters, (2009) **470**(1-3): p. 107-111.

[49] Zeng, J.-L., et al., *Effects of copper nanowires on the properties of an organic phase change material.* Solar Energy Materials and Solar Cells, (2012) **105**: p. 174-178.

[50] Ho, C.J. and J.Y. Gao, *Preparation and thermophysical properties of nanoparticle-in-paraffin emulsion as phase change material.* International Communications in Heat and Mass Transfer, (2009) **36**: p. 467-470.

[51] Choi, S.U.S. and J.A. Eastman. *Enhancing thermal conductivity of fluids with nanoparticles*. in *ASME International Mechanical Engineering Congress & Exposition*. 1995. San Francisco, CA.

[52] Wu, J.M. and J. Zhao, *A review of nanofluid heat transfer and critical heat flux enhancement--Research gap to engineering application.* Progress in Nuclear Energy, (2013) **66**: p. 13-24.

[53] Yu, W., et al., *Review and Comparison of Nanofluid Thermal Conductivity and Heat Transfer Enhancements.* Heat Transfer Engineering, (2008) **29**(5): p. 432-460.

[54] Putnam, S.A., et al., *Thermal conductivity of nanoparticle suspensions.* Journal of Applied Physics, (2006) **99**(8): p. 084308.

[55] Zhang, X., H. Gu, and M. Fujii, *Effective thermal conductivity and thermal diffusivity of nanofluids containing spherical and cylindrical nanoparticles.* Journal of Applied Physics, (2006) **100**(4): p. 044325.

[56] Li, C.H. and G.P. Peterson, *Experimental investigation of temperature and volume fraction variations on the effective thermal conductivity of nanoparticle suspensions (nanofluids).* Journal of Applied Physics, (2006) **99**(8): p. 084314.

[57] Das, S.K., et al., *Temperature Dependence of Thermal Conductivity Enhancement for Nanofluids.* Journal of Heat Transfer, (2003) **125**(4): p. 567.

[58] Xie, H., et al., *Thermal conductivity enhancement of suspensions containing nanosized alumina particles.* Journal of Applied Physics, (2002) **91**(7): p. 4568.

[59] McCartney, L.N. and A. Kelly, *Maxwell's far-field methodology applied to the prediction of properties of multi-phase isotropic particulate composites.* Proceedings of the Royal Society A: Mathematical, Physical and Engineering Sciences, (2008) **464**(2090): p. 423-446.

[60] Shenogin, S., *Role of thermal boundary resistance on the heat flow in carbon-nanotube composites.* Journal of Applied Physics, (2004) **95**(12): p. 8136.

[61] Wang, J., H. Xie, and Z. Xin, *Thermal properties of paraffin based composites containing multi-walled carbon nanotubes.* Thermochimica Acta, (2009) **488**(1-2): p. 39-42.

[62] Xie, H., W. Yu, and Y. Li, *Thermal performance enhancement in nanofluids containing diamond nanoparticles.* Journal of Physics D: Applied Physics, (2009) **42**(9): p. 095413.

[63] Abareshi, M., et al., *Fabrication, characterization and measurement of thermal conductivity of Fe3O4 nanofluids.* Journal of Magnetism and Magnetic Materials, (2010) **322**(24): p. 3895-3901.

[64] Chiesa, M. and A.J. Simonsen, *The Importance of Suspension Stability for the Hot-wire Measurements of Thermal Conductivity of Colloidal Suspensions*, in *16th Australasian Fluid Mechanics Conference*2007: Crown Plaza, Gold Coast, Australia. p. 1154-1157.

[65] Li, X.F., et al., *Thermal conductivity enhancement dependent pH and chemical surfactant for Cu-H2O nanofluids.* Thermochimica Acta, (2008) **469**(1-2): p. 98-103.

[66] Hwang, Y., et al., *Production and dispersion stability of nanoparticles in nanofluids.* Powder Technology, (2008) **186**(2): p. 145-153.

[67] Chazhengina, S.Y., et al., *Phase transitions of n-alkanes as rotator crystals.* Journal of Molecular Structure, (2003) **647**: p. 243-257.

[68] Ukrainczyk, N., S. Kurajica, and J. Šipušić, *Thermophysical comparison of five commercial paraffin waxes as latent heat storage materials.* Chemical & Biochemical Engineering Quarterly, (2010) **24**(2): p. 129-137.

[69] Parker, W.J., et al., *Flash Method of Determining Thermal Diffusivity, Heat Capacity, and Thermal Conductivity.* Journal of Applied Physics, (1961) **32**(9): p. 1679.

[70] Cape, J.A. and G.W. Lehman, *Temperature and Finite Pulse-Time Effects in the Flash Method for Measuring Thermal Diffusivity.* Journal of Applied Physics, (1963) **34**(7): p. 1909.

[71] Baba, T. and A. Ono, *Improvement of the laser flash method to reduce uncertainty in thermal diffusivity measurements.* Measurement Science and Technology, (2011) **12**: p. 12.

[72] Carslaw, H.S. and J.C. Jaeger, *Conduction of Heat in Solids*. 2nd ed2005: Oxford Science Publications.

[73] Incropera, F.P., et al., *Fundamentals of Heat and Mass Transfer* 6th ed2007: John Wiley & Sons.

[74] Yang, D., et al., *Thermal conductivity of multiwalled carbon nanotubes.* Physical Review B, (2002) **66**(16).

[75] Vadasz, P., *Rendering the Transient Hot Wire Experimental Method for Thermal Conductivity Estimation to Two-Phase Systems—Theoretical Leading Order Results.* Journal of Heat Transfer, (2010) **132**(8): p. 081601.

[76] Einstein, A., *On the movement of small particles suspended in stationary liquids required by the molecular-kinetic theory of heat.* Ann. Phys. , (1905) **17**: p. 549-560.

[77] Perrin, J., *Atoms*1916, London: Constable.

[78] Lemons, D.S., *Paul Langevin's 1908 paper "On the Theory of Brownian Motion" ["Sur la théorie du mouvement brownien," C. R. Acad. Sci. (Paris) 146, 530–533 (1908)]*. American Journal of Physics, (1997) **65**(11): p. 1079.

[79] Li, T., et al., *Measurement of the instantaneous velocity of a Brownian particle.* Science, (2010) **328**(5986): p. 1673-5.

[80] Smoluchowski, M.v., *Three discourses on diffusion, Brownian movements, and the coagulation of colloid particles.* Phys. Zeits, (1916) (17): p. 557-565.

[81] Bandyopadhyaya, R., R. Kumar, and K.S. Gandhi, *Modeling of $CaCO_3$ Nanoparticle Formation During Overbasing of Lubricating Oil Additives.* Langmuir, (2001) **17**: p. 1015-1029.

[82] Seyer, W.F., R.F. Patterson, and J.L. Keays, *The Density and Transition Points of the n-Paraffin Hydrocarbons.* Journal of the American Chemical Society, (1944) **66**(2): p. 179-182.

[83] Prasher, R., et al., *Effect of aggregation on thermal conduction in colloidal nanofluids.* Applied Physics Letters, (2006) **89**(14): p. 143119.

[84] Wang, B.-X., L.-P. Zhou, and X.-F. Peng, *A fractal model for predicting the effective thermal conductivity of liquid with suspension of nanoparticles.* International Journal of Heat and Mass Transfer, (2003) **46**(14): p. 2665-2672.

[85] Potanin, A. and W. Russel, *Fractal model of consolidation of weakly aggregated colloidal dispersions.* Physical Review E, (1996) **53**(4): p. 3702-3709.

[86] Alexiades, V. and A.D. Solomon, *Mathematical Modeling of Melting and Freezing Processes*1993, Washington DC: Hemisphere.

Appendix

A.1 Matlab Code

A.1.1 Nanofluid Effective Medium Theory

```
% file: nanofluidEMT.m
% Measuring nanofluid thermal properties from effective medium theory
% Aitor Zabalegui
% Created: 1/31/2012
% Last Updated: 6/26/2013

clc
clf
clear all

%% Nanofluid properties
% Nanofluid thermal conductivity (k)
Kp=14.5;                              %k of nanoparticles [W/m*K]
KbL=0.163;                            %k of liquid base fluid [W/m*K]
KbS=0.145;                            %k of solid base fluid [W/m*K]

% Volume fraction
phifract=0:0.1:1;
phi=phifract./100;                    %particle volume fraction

%% Maxwell's 3phi limit
KeS3phi=KbS.*(1+3.*phi);

%% Nan et al.'s EMT
%nanoparticle geometry (prolate spheroid)
a33=6.5e-6;                           %major axis (particle length) [m]
a11=15.5e-9;                          %minor axis (particle diameter) [m]
p=a33/a11;

%Kapitza thermal interface resistance
Rbd=1e-8;                             %Kapitza resistance [m^2*K/W]

L11=p^2/(2*(p^2-1))-(p/(2*(p^2-1)^(3/2)))*acosh(p);
L33=1-2*L11;

%Solid state
gammaS=((2+(1/p))*Rbd*KbS)/(a11/2);
K11CS=Kp/(1+gammaS*L33*(Kp/KbS));
K33CS=Kp/(1+gammaS*L33*(Kp/KbS));
B11S=(K11CS-KbS)/(KbS+L11*(K11CS-KbS));
B33S=(K33CS-KbS)/(KbS+L33*(K33CS-KbS));

%Liquid state
gammaL=((2+(1/p))*Rbd*KbL)/(a11/2);
K11CL=Kp/(1+gammaL*L33*(Kp/KbL));
```

```
K33CL=Kp/(1+gammaL*L33*(Kp/KbL));
B11L=(K11CL-KbL)/(KbL+L11*(K11CL-KbL));
B33L=(K33CL-KbL)/(KbL+L33*(K33CL-KbL));

%Effective nanofluid TC
KeS=KbS.*((3+phi.*(2*B11S*(1-L11)+B33S*(1-L33))./(3-
phi.*(2*B11S*L11+B33S*L33)));                          %Solid
KeL=KbL.*((3+phi.*(2*B11L*(1-L11)+B33L*(1-L33))./(3-
phi.*(2*B11L*L11+B33L*L33)));                          %Liquid

%% Hashin-Shtrikman (H-S) theoretical k bounds
Khslow=KbS.*(1+((3.*phi.*(Kp-KbS))./(3*KbS+(1-phi).*(Kp-KbS))));
Khshigh=Kp.*(1-((3.*(1-phi).*(Kp-KbS))./(3*Kp-phi.*(Kp-KbS))));

%% Hamilton-Crosser (H-C) effective k for spherical/cylindrical
particles
ns=3;
nc=6;
Khc_s=KbS*(Kp+KbS*(ns-1)-phi.*(KbS-Kp)*(ns-1))./(Kp+KbS*(ns-
1)+phi.*(KbS-Kp));
Khc_c=KbS*(Kp+KbS*(nc-1)-phi.*(KbS-Kp)*(nc-1))./(Kp+KbS*(nc-
1)+phi.*(KbS-Kp));

%% EMT plots
subplot(3,1,1),plot(phifract,KeS3phi./KbS,'b',phifract,KeS./KbS,'r',phi
fract,Khslow./KbS,'-.c',phifract,Khshigh./KbS,'k',phifract,Khc_c./KbS,
'--k',phifract,Khc_s./KbS,'--g')
ylabel('k_{nf}/k_{bf}')
legend('Maxwell 3\phi limit','Nan et al.','H-S low','H-S high','H-C
Sphere','H-C Cylinder')
title('NF thermal conductivity w.r.t. particle volume fraction')

%% Nanofluid density EMT (rho)
rhonp=2.1;                                %np true density [g/cm^3]
rhobf=0.897925;                           %bf solid density [g/cm^3]
rhobfL=0.78;                              %bf liquid density [g/cm^3]
rhonf=((1-phi).*rhobf)+(phi.*rhonp);      %nf solid density [g/cm^3]
rhonfL=((1-phi).*rhobfL)+(phi.*rhonp);    %nf liquid density [g/cm^3]

%% Nanofluid specific heat (Cp)
Cpnp=0.460;                               %np Cp [J/gK]
Cpbf=1.888;                               %bf solid Cp [J/gK]
CpbfL=1.298;                              %bf liq. Cp [J/gK]
Cpnf=(((1-phi).*rhobf*Cpbf)+(phi.*rhonp*Cpnp))./rhonf; %nf Cp [J/gK]
CpnfL=(((1-phi).*rhobfL*CpbfL)+(phi.*rhonp*Cpnp))./rhonfL;

subplot(3,1,2), plot(phifract,Cpnf./Cpbf)
ylabel('Cp_{nf}/Cp_{bf}')
title('NF specific heat w.r.t. particle volume fraction')

%% Nanofluid thermal diffusivity (alpha)
alphanf=KeS./(Cpnf.*rhonf);
alphabf=alphanf(1);
alpha3phi=KeS3phi./(Cpnf.*rhonf);
```

```
subplot(3,1,3),
plot(phifract,alpha3phi./alphabf,'b',phifract,alphanf./alphabf,'r')
xlabel('\phi_{p}[%]')
ylabel('\alpha_{nf}/\alpha_{bf}')
legend('Maxwell 3\phi limit','Nan et al.')
title('NF thermal diffusivity w.r.t. particle volume fraction')
```

A.1.2 Nanofluid Fabrication and Sample Density Measurement

```
%file: fabanddensity.m
%Calculate sample density and nanoparticle weight for desired phi
%Aitor Zabalegui
%Created: 7/17/2012
%Last updated: 6/26/2013

clc
clear all

%Desired particle volume fraction
phi=0.01;

%Properties of base fluid (bf), nanoparticles (np), and nanofluid (emt)
Wbf=7.7515;                                    %measured bf weight[g]
rhobfl=0.7796;                                 %bf liq. density [g/cm^3]
rhobfs=0.895333;                               %bf solid density [g/cm^3]
rhonptrue=2.1;                                 %np true density [g/cm^3]
Wnp=(phi.*rhonptrue*Wbf)./(rhobfl.*(1-phi)); %measured np weight [g]
rhoemts=phi*rhonptrue+(1-phi).*rhobfs;         %nf solid density [g/cm^3]

%Convert weight fraction to volume fraction
wf=((phi.*rhonptrue)./(phi.*rhonptrue+rhobfl.*(1-phi)));

%Density approximation (Archimedes' kit)
Wa=0.0465;                                    %sample weight in air [g]
Ww=-0.0052;                                   %sample weight in fluid[g]
rhonf=(Wa/(Wa-Ww))*(0.9978-0.0012)+0.0012;  %sample density [g/cm^3]
```